

DOCTORAL THESIS

Thesis Title

Author:

Ana ANDRES-ARROYO

Supervisor:

Dr. First LAST

A thesis submitted in fulfilment of the requirements for the degree of
Doctor of Philosophy



UNSW
AUSTRALIA

School of Physics, Faculty of Science

November 2018

Dedicated to someone.

“Fancy Quote”

Author

Abstract

School of Physics, Faculty of Science, UNSW Australia

Doctor of Philosophy

Thesis Title

by Ana ANDRES-ARROYO

Write your abstract here .

Acknowledgements

The acknowledgements and the people to thank go here, don't forget to include your project advisor...

Contents

Dedication	iii
Quotation	v
Abstract	vii
Acknowledgements	viii
Contents	ix
List of Figures	xi
Abbreviations	xiii
Physical Constants	xv
Symbols	xvii
1 Introduction	1
1.1 Section title	2
1.2 Compiling instructions	2
1.3 References	2
2 Using Fourier transform phase for the measurement of radial velocity	3
2.1 Phase analysis of Fourier transform for the measurement of line shift	6
2.1.1 Translation property of Fourier transform	6
2.1.2 Intuitive explanation	6
2.1.3 Practical Use	7
2.1.4 Initial tests to obtain RV_{FT}	8
2.1.5 Further tests to obtain $RV_{FT,H}$ and $RV_{FT,L}$	11
2.1.6 Cut-off frequency	13
2.1.7 Conclusion	14
2.2 Using the Fourier transform to probe line deformation	15
2.2.1 Theory	15
2.2.2 SOAP simulations	16
2.2.3 Fourier phase spectrum analysis	17
2.2.3.1 RV_{FT}	17
2.2.3.2 $RV_{FT,H}$ and $RV_{FT,L}$	18

2.2.4	Jitter model	20
2.2.5	Testing the recovery of jitter	22
	Weighted moving average	22
2.2.6	Planetary radial velocity recovery	25
2.2.7	Conclusion	26
2.3	End-to-end simulations	27
2.3.1	Stellar jitter as strong as planetary signal	28
2.3.2	Planetary signal dominates	30
2.3.3	Stellar jitter only	32
2.3.4	Classification	33
2.3.5	Periogogram combined with the Φ ESTA	35
2.4	Applying Φ ESTA on real observations	36
2.4.1	HD189733: Rossiter–McLaughlin effect as jitter	36
2.4.2	α Centauri B (HD128621)	38
2.4.3	ϵ Eridani (HD22049)	41
2.4.4	τ Ceti (HD10700)	41
2.5	References	42

List of Figures

1	Introduction	1
2	Using Fourier transform phase for the measurement of radial velocity	3
2.1	Simulation map	5
2.2	Translation property of Fourier transform	8
2.3	100 shifted HARPS-like line profiles	9
2.4	Fourier transform of 100 shifted line profiles	9
2.5	Radial velocity recovery	10
2.6	Low-pass and high-pass filters	12
2.7	Low-pass and high-pass radial velocities	12
2.8	Fourier transform of a line profile in a complex plane	13
2.9	Deformed line profile	16
2.10	Fourier transform of deformed line profiles	17
2.11	Apparent RV of deformed line profiles	18
2.12	Low-pass and high-pass filters	19
2.13	Fourier transform in response to line deformation	19
2.14	Scaling the low-pass and high-pass Fourier transformed radial velocities .	20
2.15	Jitter model	23
2.16	Corner plots of MCMC	28
2.17	Planet recovery ($A = 2 \text{ m/s}$)	29
2.18	Histograms of recovered orbital parameters ($A = 2 \text{ m/s}$)	30
2.19	Planet recovery ($A = 20 \text{ m/s}$)	31
2.20	Histogram of recovered orbital parameters ($A = 20 \text{ m/s}$)	32
2.21	Histogram of recovered orbital parameters of null planets	33
2.22	Classification of jitter dominated or planetary signal dominated	34
2.23	Periodogram combined with Φ ESTA	35
2.24	Demo: Rossiter–McLaughlin effect	36
2.25	HD189733: modelling Rossiter–McLaughlin effect as jitter	37
2.26	α Centauri B: stellar activity analysis	40

Abbreviations

2D Two-Dimensional

3D Three-Dimensional

Physical Constants

Speed of Light $c = 2.997\ 924\ 58 \times 10^8\ \text{ms}^{-1}$ (exact)

Constant Name Symbol = Constant Value (with units)

Symbols

f	focal length	mm or cm
H	heating	K/W
I	intensity	a.u.
k	trap stiffness	pN/ μ m/mW
n	refractive index	—
P	power	mW
T	temperature	°C or K
ε	permittivity	???
κ	trap stiffness	pN/ μ m/mW
λ	wavelength	nm
μ	permeability	???
σ	cross section	???
θ	tilt angle	degrees or radians

¹ Chapter 1

Introduction

1.1	Section title	2
1.2	Compiling instructions	2
1.3	References	2

1.1 Section title

Always put `labelthesection` after each section so the page headers work.

This is a test.

1.2 Compiling instructions

1. make the main file the master document: options `-j` make current file master document
2. Quick build from anywhere (because it quick builds from the master document)
3. BibTex from the chapter file (disable the master document option for this and do it from "normal mode")
4. Quick build 3 times (from the master document): 1 for the text, 2 for the references and labels, 3 for the bibliography backreferencing.

1.3 References

¹ Chapter 2

Using Fourier transform phase for the measurement of radial velocity

2.1	Phase analysis of Fourier transform for the measurement of line shift	6
2.1.1	Translation property of Fourier transform	6
2.1.2	Intuitive explanation	6
2.1.3	Practical Use	7
2.1.4	Initial tests to obtain RV_{FT}	8
2.1.5	Further tests to obtain $RV_{FT,H}$ and $RV_{FT,L}$	11
2.1.6	Cut-off frequency	13
2.1.7	Conclusion	14
2.2	Using the Fourier transform to probe line deformation	15
2.2.1	Theory	15
2.2.2	SOAP simulations	16
2.2.3	Fourier phase spectrum analysis	17
2.2.3.1	RV_{FT}	17
2.2.3.2	$RV_{FT,H}$ and $RV_{FT,L}$	18
2.2.4	Jitter model	20
2.2.5	Testing the recovery of jitter	22
Weighted moving average	22
2.2.6	Planetary radial velocity recovery	25
2.2.7	Conclusion	26

2.3	End-to-end simulations	27
2.3.1	Stellar jitter as strong as planetary signal	28
2.3.2	Planetary signal dominates	30
2.3.3	Stellar jitter only	32
2.3.4	Classification	33
2.3.5	Periogogram combined with the ϕ ESTA	35
2.4	Applying ϕESTA on real observations	36
2.4.1	HD189733: Rossiter–McLaughlin effect as jitter	36
2.4.2	α Centauri B (HD128621)	38
2.4.3	ϵ Eridani (HD22049)	41
2.4.4	τ Ceti (HD10700)	41
2.5	References	42

This chapter introduces a new method for measuring radial velocities. Specifically, it uses the Fourier transform of a line profile (or cross-correlation profile) to distinguish between the effects of a bulk shift in that profile (i.e. a radial velocity shift of the profile), as opposed to a change in the line profile shape which can produce an apparent radial velocity shift. We examine the impact on the Fourier transformed components of a line profile of both bulk line shifts, and line profile deformations, with the aim of developing tools to distinguish between these two cases.

There are a lot of simulations involved apart from laying out theories and building up models. The following diagram shows a quick roadmap of the tests made with the newly proposed technique – Fourier transform phase analysis, and how the simulations are organized in the chapter, for future reference.

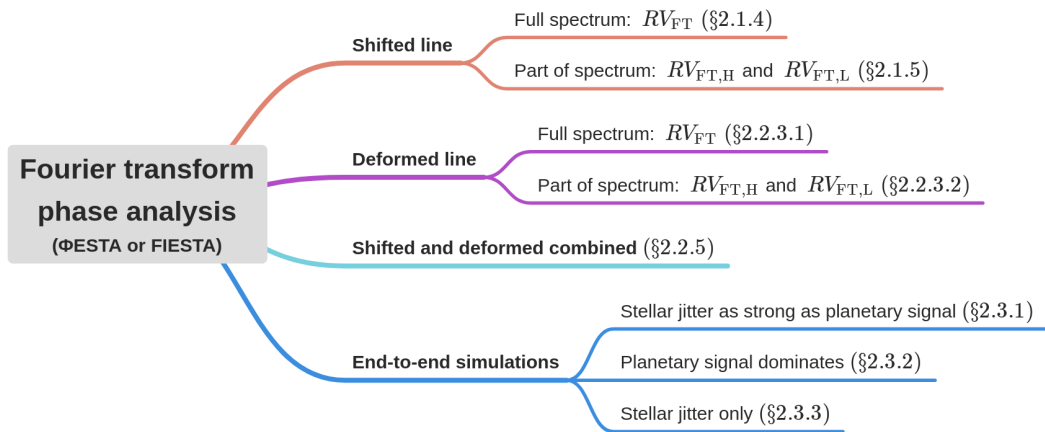


Fig. 2.1: Roadmap of Fourier transform phase analysis on simulated data.

2.1 Phase analysis of Fourier transform for the measurement of line shift

The translation of a function (in our case a spectral line profile) can be examined in both its original real space, and in its Fourier transformed space. Because Fourier transform is often used to handle time domain data, a shift in real space can be variously described as either time shifting or translation. In this chapter we will use “time shifting”, “translation” and “velocity shifting” interchangeably to refer to a shift of a function in real space. We will refer to Fourier transformed functions as being in the “frequency domain” regardless of whether they have actual dimensions of 1/time, 1/length or 1/velocity.

2.1.1 Translation property of Fourier transform

Let us consider a function $h(x)$ as a signal $f(x)$ delayed (or shifted) by an amount x_0 :

$$h(x) = f(x - x_0). \quad (2.1)$$

In the frequency domain, we will then have

$$\hat{h}(\xi) = e^{-2\pi i x_0 \xi} \hat{f}(\xi), \quad (2.2)$$

where the circumflex denotes the Fourier transform of a function, i.e.

$$\hat{f}(\xi) = \int_{-\infty}^{\infty} f(x) e^{-2\pi i x \xi} dx. \quad (2.3)$$

E.q. 2.2 means that while the power spectrum remains unchanged for shifted signals, i.e. $|\hat{h}(\xi)|^2 = |\hat{f}(\xi)|^2$, the phases $\phi(\xi)$, defined as the argument of the Fourier representation $\hat{f}(\xi)$: $\text{Arg}(\hat{f}(\xi))$, have changed because of the additional term $e^{-2\pi i x_0 \xi}$. The extra phases $\Delta\phi(\xi)$ added are:

$$\Delta\phi(\xi) = -2\pi x_0 \xi. \quad (2.4)$$

2.1.2 Intuitive explanation

An intuitive, but equally quantitative way, to see how E.q.2.4 holds is as follows. The Fourier transform decomposes the function $f(x)$ into a frequency representation $\hat{f}(\xi)$,

accompanied by the orthogonal basis $e^{2\pi i x \xi}$, as in the form of inverse Fourier transform:

$$f(x) = \int_{-\infty}^{\infty} \hat{f}(\xi) e^{2\pi i x \xi} d\xi. \quad (2.5)$$

Shifting $f(x)$ by x_0 is equivalent to shifting *all* the orthogonal basis functions by x_0 , which then become $e^{2\pi i (x-x_0) \xi} = e^{2\pi i x \xi} \cdot e^{-2\pi i x_0 \xi}$. This is how the additional term $e^{-2\pi i x_0 \xi}$ in Eq. 2.2 arises – it quantifies the phase difference for a shifted function.

An even more intuitive but less quantitative way to envision the relation between a shift of the signal and a phase difference is to imagine any real continuous function is a sum of sines and cosines. Changing the phase angle in the sines and cosines results in shifts in the function.

The power spectrum of such a shifted function remains the same because shifting the signal as a whole doesn't add or remove any frequency components.

2.1.3 Practical Use

From Eq. 2.4, we see that the phase shift $\Delta\phi(\xi)$ is proportional to the frequency ξ with a constant gradient or slope

$$\frac{d(\Delta\phi)}{d\xi} = -2\pi x_0 \quad (2.6)$$

where Δ is used to refer to the phase difference between a shifted line profile and an unshifted / referenced line profile, while the derivative refers to the response of $\Delta\phi(\xi)$ to ξ . $\Delta\phi(\xi)$ is measured as the change in phases $\text{Arz}(\hat{h}(\xi)) - \text{Arz}(\hat{f}(\xi))$. Then a linear regression model can be fit to a plot of $\Delta\phi(\xi)$ versus ξ (Fig. 2.2) to enable measurement of the bulk shift between two line profiles x_0 .

By analogy with the definition of power spectrum, we describe $\phi(\xi)$ as the **phase spectrum** and hence $\Delta\phi(\xi)$ as the **differential phase spectrum**. In this approach, an analysis of the phase shift in the frequency domain of the Fourier components of a line profile will provide a means of measuring a bulk line shift in real space. We therefore name our method **FourIER phase SpecTrum Analysis** (Φ ESTA or FIESTA).

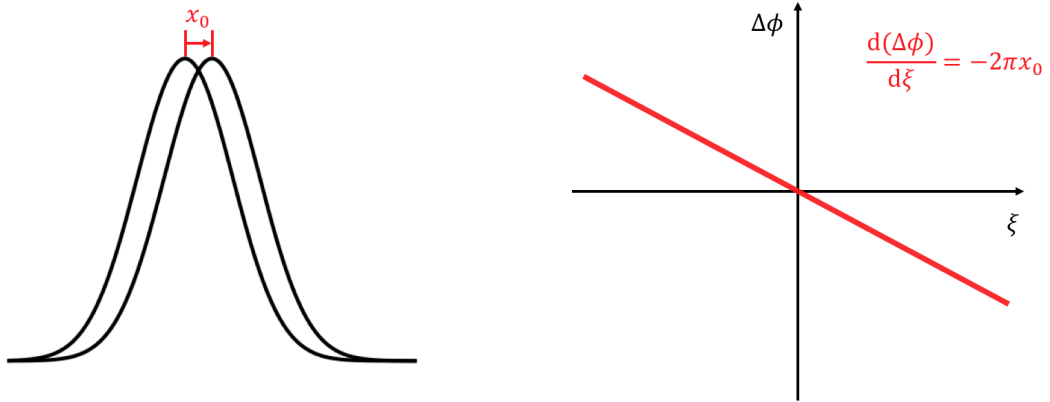


Fig. 2.2: The left panel shows a signal (or a spectral line profile in the following context) shifted by an amount x_0 . The right panel is the differential phase spectral density diagram (i.e. differential phase spectrum). The model shows the phase difference between two shifted signals $\Delta\phi(\xi)$ and the frequency ξ are linearly correlated. Its slope $-2\pi x_0$ contains information of the amount of signal shift in time domain.

2.1.4 Initial tests to obtain RV_{FT}

We performed an initial test to determine that we can correctly recover known shifts of a line profile using Φ ESTA. We generated a spectral line profile based on the cross-correlation function of observed HARPS spectra with the software SOAP 2.0 [1]. This was replicated 100 times, with a very small amount of noise (equivalent to a S/N = 10,000) injected in each of the line profiles. These profiles were then subjected to radial velocity shifts evenly spaced between 0 and 10 m/s (Fig. 2.3).

The Fourier transform of these 100 spectral line profiles divides the information into two parts: (1) the power spectra (Fig. 2.4a) and (2) the phase spectra (shown in Fig. 2.4b as the differential phase spectra relative to the phase spectrum of the unshifted line profile). We see that most information is concentrated towards the centre of the power spectrum (i.e. the lower frequency range), and as expected, the differential phase spectra are mostly linear, consistent with the theory demonstrated in Fig. 2.2. Deviations from linearity come from the noise that we injected, which will be discussed later.

The slope of each differential phase spectrum indicates the shift of each line profile relative to the unshifted one. For a linear regression fitting, each frequency sample on the differential phase spectrum is weighted by the amplitude of the power, meaning the lower frequencies receive more weights. We calculate the radial velocity shift for each

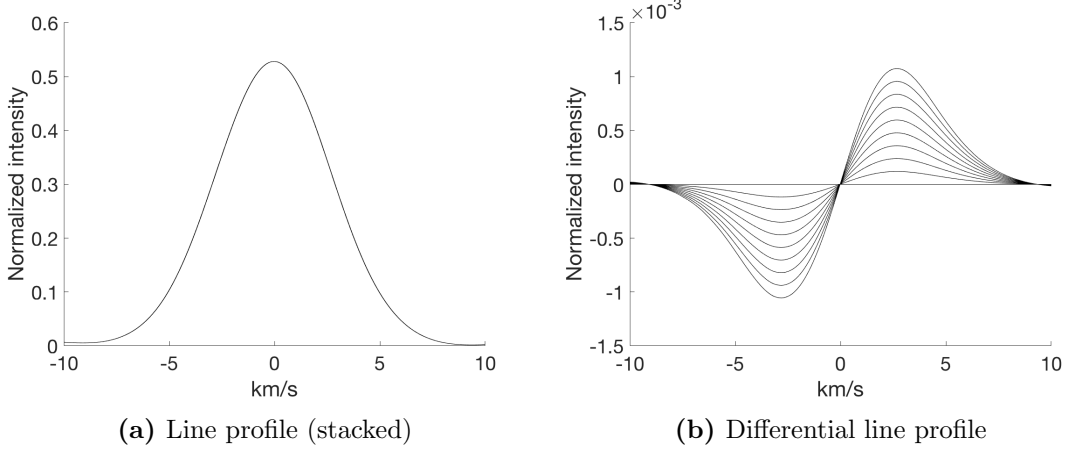


Fig. 2.3: (a) the shifted line profiles plotted on top of each other, showing that the 0-10 m/s shifts are very small compared to the line profile width. (b) the shifted line profiles with the unshifted line profile subtracted from each. Note that for the sake of clarity, the differential line profiles are plotted noise-free and only 10 out of 100 profiles are displayed.

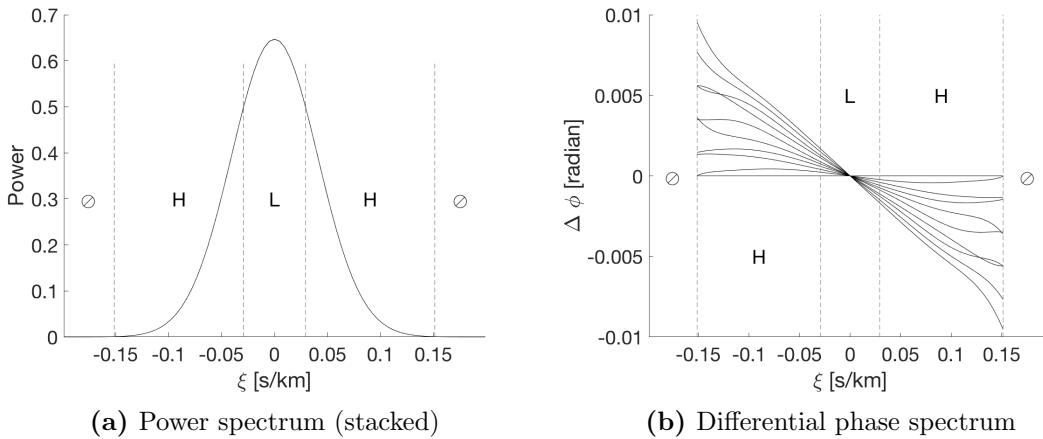


Fig. 2.4: The Fourier transform of these shifted line profile divides the information in each into (a) their power spectra and (b) their phase spectra (here plotted differential compared to that of the unshifted profile). A line shift in the time domain produces an unchanged power spectrum in the frequency domain. It does, however, produce phase shifts which we see as linear trends in the differential phase spectra as a function of frequency. Only 10 out of 100 differential phase spectra are displayed. The differential phase spectrum can be sub-divided into higher frequency range (H) and lower frequency range (L). The \emptyset region contains little power and frequency information and thus not used. We derive RV_{FT} from the full spectrum (except \emptyset), $RV_{FT,H}$ from the higher frequency range and $RV_{FT,L}$ from the lower frequency range.

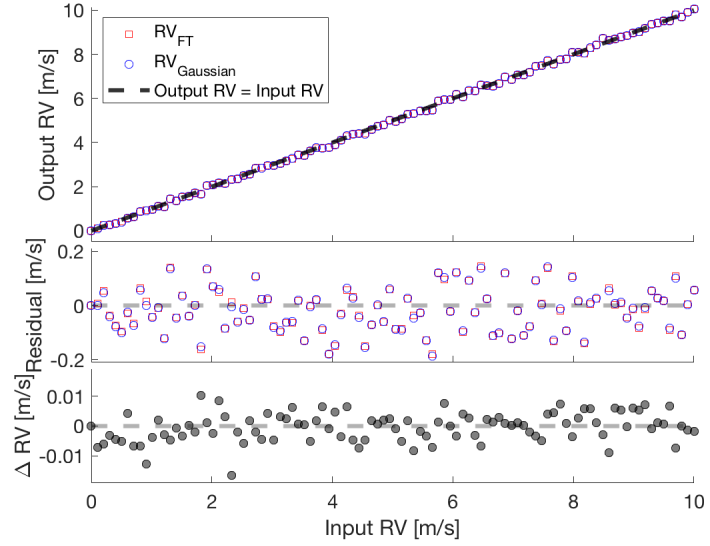


Fig. 2.5: Radial velocity recovery of line shifts with both methods: Fourier transform and Gaussian fit. Top: RV_{FT} and $RV_{Gaussian}$ plotted against the input radial velocity shifts. Middle: residuals as RV_{FT} and $RV_{Gaussian}$ subtracted by the input radial velocity shifts. Bottom: ΔRV defined as the difference between RV_{FT} and $RV_{Gaussian}$, showing the highly consistency between each other. Note that axes scales are different across the subplots; errorbars are estimated to be the size of scatter 0.08 m/s but are not plotted for clarity.

shifted line profile using two methods: (1) Φ ESTA to determine RV_{FT} ; (2) traditional measurement of the line centroid by fitting a Gaussian function to each line profile that delivers $RV_{Gaussian}$.

We then compare both RV_{FT} and $RV_{Gaussian}$ with the known input line shift. Fig. 2.5 reveals the expected 1:1 correlation between the input radial velocity shift and the output – the line of best fit of a linear regression model presents a slope of 1.003 ± 0.006 with 95% confidence bounds for both RV_{FT} and $RV_{Gaussian}$. The root-mean-square (rms) of the residuals (or interchangeably used as standard deviation when the mean is zero) are both $\sigma_{FT} = \sigma_{Gaussian} = 0.08$ m/s, identical up to two decimal places, indicating the expected radial velocities are consistently obtained by both methods. In fact, the almost overlapping residuals in Fig. 2.5 middle panel means that the two methods are so coherently different from the input radial velocity (by small amounts) that this scatter must come from the photon noise intrinsic to the simulated line profiles rather than the methods themselves.

CGT: How do these compare which what you'd expect from the S/N and the intrinsic line width (should say at some int what the intrinsic line width is).

2.1.5 Further tests to obtain $RV_{FT,H}$ and $RV_{FT,L}$

Let's recall the justification of measuring a line shift in its Fourier space – the shifting of a line (or a function), when viewed as shifting the sum of its Fourier basis functions (or any other basis functions), has equally the same amount of shift on every basis function, which can be measured as a phase shift in the Fourier phase spectrum. That is to say, utilising only part of the phase spectrum will also return the correct shift of a line profile, although it utilises less information. The motivation of this will be discussed in §2.2 when we look at line profile deformations.

We divide the whole frequency range available into two parts (Fig. 2.4) – a lower frequency range (i.e. apply a low-pass filter) and a higher frequency range (i.e. apply a high-pass filter). The dividing frequency ξ_{HL} can be chosen arbitrarily for the time being, for example, such that both the lower and higher frequency ranges take up half of the power spectrum $P(\xi)$:

$$\int_{\xi_L=0}^{\xi_{HL}} P(\xi) d\xi = \int_{\xi_{HL}}^{\xi_H} P(\xi) d\xi. \quad (2.7)$$

We assume here that the integration of the power spectrum measures the amount of “information” in the original line profile, so that in a noise-free circumstance, we would put equal trust on the radial velocities obtained from the lower and higher frequencies (namely $RV_{FT,L}$ and $RV_{FT,H}$, or $RV_{FT,H/L}$ for both). In addition, a cut-off frequency ξ_H is applied to the upper boundary of the high-pass filter (so is $-\xi_H$ on the negative part). Frequencies higher than ξ_H hardly contributes to the shape of the line profile as $P(\xi)$ converges to zero, and they can be impacted by noise in an unpredictable way. ξ_H is chosen empirically where $P(\xi)$ drops to 0.1% of $\max\{P(\xi)\}$.

We presented in Fig. 2.5 an accurate recovery of the radial velocity shift given by RV_{FT} , for which the full range of frequencies were used; For comparison in Fig. 2.7, it still delivers a good 1:1 alignment between $RV_{FT,H/L}$ and the input radial velocities. The line of best fit presents a slope of 1.002 ± 0.007 for $RV_{FT,L}$ and 0.977 ± 0.029 for $RV_{FT,H}$ respectively, with 95% confidence bounds. The scatter of the residuals are $\sigma_{FT,L} = 0.11$ m/s and $\sigma_{FT,H} = 0.43$ m/s. First, we note that $\sigma_{FT,H/L} > \sigma_{FT}$, this is because both $RV_{FT,H}$ and $RV_{FT,L}$ are derived from part of information in the Fourier space. Second, we note that $\sigma_{FT,H} > \sigma_{FT,L}$, seemingly contradicting with the expectation that equal amount of “information” from which they are derived should deliver the equivalent amount of scatter in the residuals. We think this may be because higher frequency

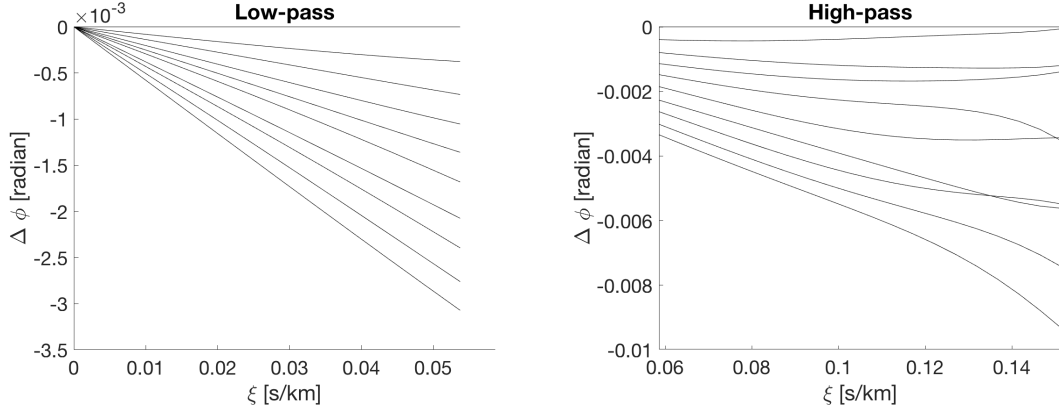


Fig. 2.6: Differential phase spectrum as shown in Fig. 2.4b sub-divided into lower frequency range and higher frequency range. Only the non-negative ranges are plotted.

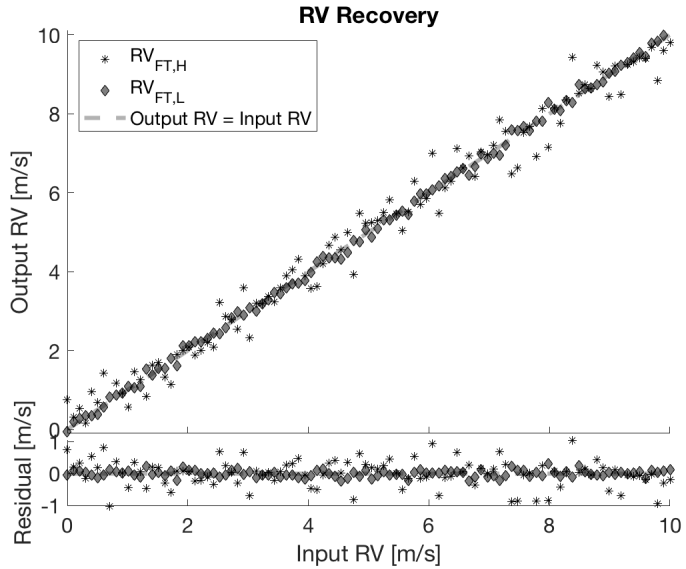


Fig. 2.7: Radial velocity recovery of line shifts with low-pass and high-pass filters. Errorbars are not plotted for clarity.

modes are more likely to be subjected to stochastic behaviours other than the line deformation arising from stellar variability generated in the SOAP model. For example, the fluctuations of photon levels on the stellar spectrum are mainly described by high frequency modes. *jzhao: Have I made myself clear here?*

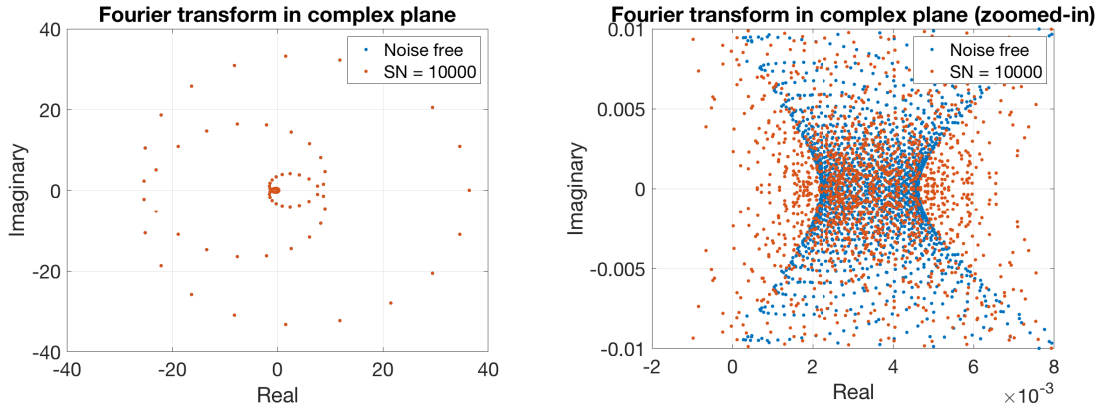


Fig. 2.8: The Fourier transform of a line profile in a complex plane. The right figure is a zoom-in of the left near the origin.

2.1.6 Cut-off frequency

We briefly mentioned in §2.1.4 that deviation from linearity in the differential phase spectrum arises from the photon noise injected in the simulated line profiles, and in §2.1.5 that introducing a cut-off frequency in the upper boundary avoids dealing with noise. This can be visually explained with the Fourier transformed line profile $\hat{h}(\xi)$ in a complex plane (also known as the Argand plane; Fig. 2.8). For each complex number $\hat{h}(\xi)$, the argument returns the phase angle and the square of the absolute value returns the power. For larger powers (i.e. $\hat{h}(\xi)$ far from the origin as viewed in Fig. 2.8 left), the presence of noise ($S/N = 10,000$) barely alters the phase angle; for lower powers (i.e. $\hat{h}(\xi)$ distributed in the vicinity of the origin as viewed in Fig. 2.8 right), a slight displacement of $\hat{h}(\xi)$ in the complex plane means a considerable change in the phase angle in the presence of even a small amount of noise ($S/N = 10,000$). It justifies using the Fourier transform spectral power to be the weight of each frequency, and introducing a cut-off frequency when making a linear fit of the differential phase spectrum.

Another reason to introduce the cut-off frequency is the periodicity of the basis functions in a Fourier transform. The basis functions $e^{-2\pi i x_0 \xi}$ repeat themselves at the periods of $1/\xi$, making measuring the shift in the time domain larger than the order of $1/\xi$ degenerate (i.e. the shifts of $x_0 + k/\xi$ for $k \in \mathbb{Z}$ become indistinguishable). Nevertheless, this is very unlikely the case that we may encounter. In the test examples above, the cut-off frequency is $\xi = 0.15$ s/km, corresponding to the period of $1/\xi \sim 6.7$ km/s, which is way larger than the radial velocities induced by planets that we normally study at scales of m/s amplitudes.

2.1.7 Conclusion

In this section, we have introduced a new method for measuring radial velocities – Fourier phase spectrum analysis (a.k.a ϕ ESTA or FIESTA). We tested this method on shifting a simulated line profile. It confirms that using the differential Fourier phase spectrum, it is possible to measure a radial velocity to similarly high precision as to fitting a line centroid by a Gaussian profile. This provides an alternative to the traditional means of obtaining the radial velocities via centroiding the line profile in real space.

In a broader context, this method will be applicable to measuring shifts of any pattern, and can be extended to higher dimensions. In this thesis, we primarily focus on its use to measure radial velocity shifts in spectral line profiles, and especially whether the Fourier transform phase velocity is more robust against the influence of changes in line deformation than traditional techniques.

2.2 Using the Fourier transform to probe line deformation

In § 2.1, we showed that ϕ ESTA correctly measures the actual line profile shifts due to a bulk motion of the emitting star. In this section, we test whether this method is robust against spurious apparent radial velocity shifts produced by changes in the line profile shape.

2.2.1 Theory

For a line profile shifted by a small amount x_0 , the same shift x_0 applies to *all* of its basis functions. Where a line profile is changed or deformed (as opposed to simply shifted), x_0 becomes frequency dependent. That is to say, basis functions at different frequencies would be shifted by different amounts to produce shape changes (e.g. skewness, kurtosis and higher order terms) in the line profile. Therefore we modify the translation property of Fourier transform by rewriting x_0 as $x_0(\xi)$ in Eq. 2.4:

$$\Delta\phi(\xi) = -2\pi x_0(\xi)\xi. \quad (2.8)$$

As a result, the local gradient of the differential phase spectrum, instead of $-2\pi x_0$ in the case of no line profile deformation, becomes

$$\frac{d(\Delta\phi)}{d\xi} = -2\pi(x_0 + \frac{dx_0}{d\xi}). \quad (2.9)$$

Note that the dependency of ξ has been taken out of $\Delta\phi(\xi)$ and $x_0(\xi)$ in writing the differential equation above.

In principle, we could numerically solve the differential equation (either Eq. 2.8 or Eq. 2.9) based on the measured $\Delta\phi$ or local gradient $d(\Delta\phi)/d\xi$ to obtain $x_0(\xi)$, to further seek to understand which frequency modes are related to stellar variability, as distinct from frequency modes responding to a bulk shift of a line profile. As a simplistic approach, we could use an *averaged* shift $\overline{x_0(\xi)}$ to describe an overall shift of various frequency modes and rewrite Eq. 2.8 as

$$\Delta\phi(\xi) = -2\pi\overline{x_0(\xi)}\xi \quad (2.10)$$

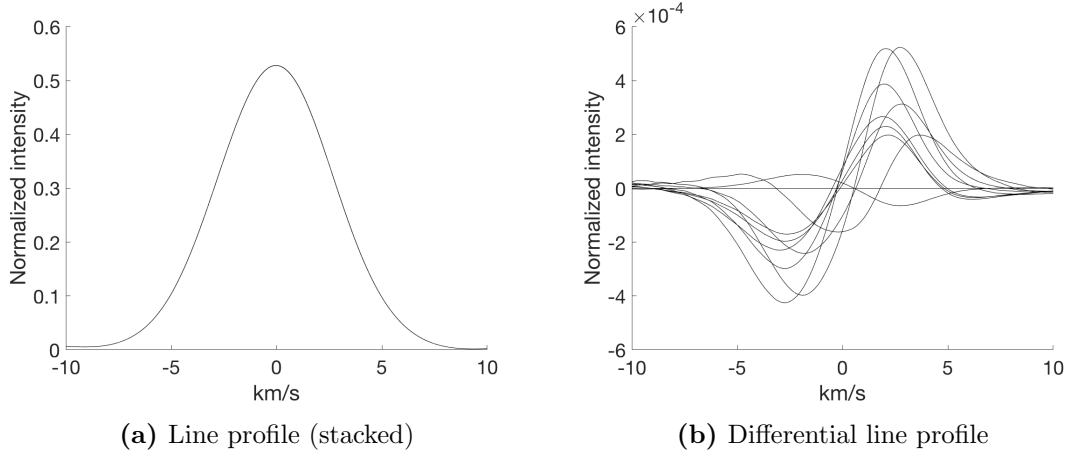


Fig. 2.9: Deformed line profile. For the sake of clarity, the differential line profiles are plotted noise-free and only 10 out of 100 profiles are presented.

where $\overline{x_0(\xi)}$ is treated as a constant for the range of frequencies that we study. Then we can study the effective line shifts in the lower frequency range versus the higher frequency range (i.e. applying a low-pass and a high-pass filter).

2.2.2 SOAP simulations

In § 2.1, we used the SOAP simulator to generate a line profile that resembles the HARPS observation to study a line shift in the Fourier space. In this section, we instead use SOAP 2.0 to study line deformations arising from starspots.

We injected three spots with different longitudes, latitudes and sizes (parameters specified in Table 2.1) to model an emitting star, and generated 100 cross-correlation functions for the resulting deformed line profiles evenly sampled throughout the rotation period of the star (Fig. 2.9). A very small amount of noise (equivalent to a S/N = 10,000) was also added into the line profiles in the simulation.

	Longitude	Latitude	Size in disk area percentage
Spot 1	174°	-14°	0.18%
Spot 2	288°	74°	0.40%
Spot 3	51°	52°	0.50%

Table 2.1: Spot configurations

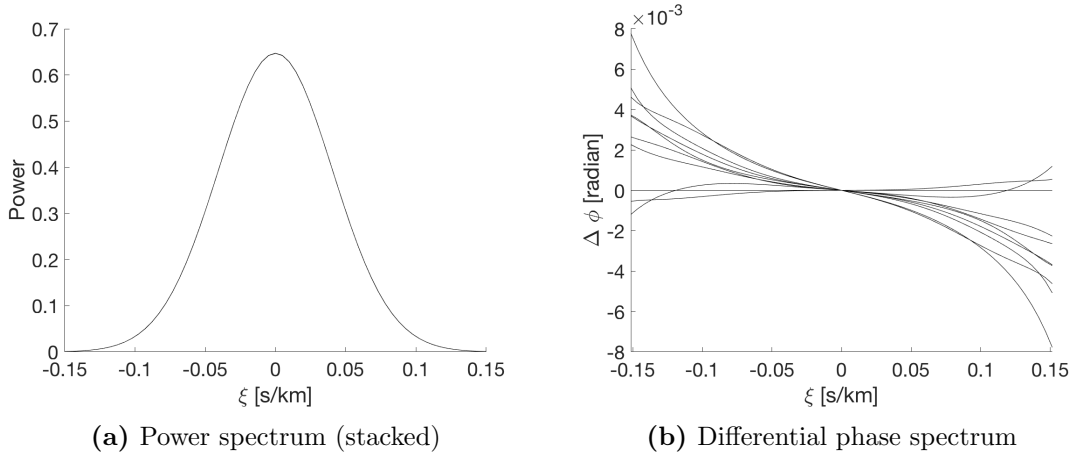


Fig. 2.10: Fourier transform of deformed line profiles. Only 10 out of 100 differential phase spectra are presented.

2.2.3 Fourier phase spectrum analysis

2.2.3.1 RV_{FT}

We then take the same approach as previously (§ 2.1) to obtain the power spectrum and the differential phase spectrum (Fig. 2.10) to measure radial velocities RV_{FT} . It is immediately apparent that a line deformation contributes to a skewed differential phase spectrum, as the the shift $x_0(\xi)$, which is related to the local gradient of the differential phase spectrum, becomes frequency dependent.

In this case, the traditionally measured radial velocities would be solely the apparent radial velocities due to deformed line profiles (a.k.a. jitter). Both velocities RV_{FT} and RV_{Gaussian} are plotted against rotation phase (Fig. 2.11). If we take $\sigma_{\text{FT}} = \sigma_{\text{Gaussian}} = 0.08$ m/s to be the intrinsic photon noise level corresponding to $S/N = 10,000$ as measured in § 2.1.4, and assume RV_{FT} and RV_{Gaussian} are independent measurements, the difference between RV_{FT} and RV_{Gaussian} would have an uncertainty of $\sqrt{\sigma_{\text{FT}}^2 + \sigma_{\text{Gaussian}}^2} \approx 0.11$ m/s. Fig. 2.11 presents $|\Delta RV| = |RV_{\text{FT}} - RV_{\text{Gaussian}}| < 0.03$ m/s. Therefore, we can see that RV_{FT} and RV_{Gaussian} are indistinguishably consistent in the measurement of the apparent radial velocities of a deformed line profile.

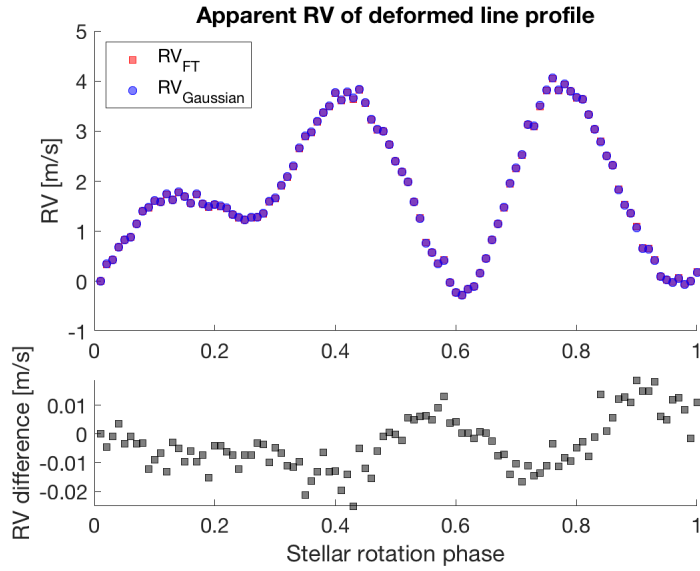


Fig. 2.11: Apparent RV of deformed line profiles calculated with both Φ ESTA and Gaussian fit to the line profile. Both results are also highly consistent with each other. $\Delta RV = RV_{\text{FT}} - RV_{\text{Gaussian}}$.

2.2.3.2 $RV_{\text{FT},\text{H}}$ and $RV_{\text{FT},\text{L}}$

Although an intrinsic line deformation (in the absence of any velocity shift in the host star) usually mimics a radial velocity shift, we note the shape differences in the differential phase spectrum between an actual line shift (Fig. 2.4b) and a line deformation (Fig. 2.10b) – the latter presents slightly flatter features in lower frequencies and becomes more skewed towards higher frequencies. Such differences provide key information for differentiating the two situations.

According to §2.2.1 where we introduced $\overline{x_0(\xi)}$ – an averaged shift for a particular frequency range – we compute the equivalent radial velocity shift for each of the lower and higher frequency ranges (Fig. 2.12). We present our results by plotting the obtained $RV_{\text{FT},\text{H/L}}$ against the jitter (line centroid fitted by a Gaussian profile) in Fig. 2.13. The $RV_{\text{FT},\text{H}}$ and $RV_{\text{FT},\text{L}}$ are both linearly correlated with the jitter though with different slopes. Fitting with a linear regression model, it comes with a slope $k_{\text{H}} = 1.978 \pm 0.100$ ($\pm 5.1\%$) for $RV_{\text{FT},\text{H}}$, meaning an apparent radial velocity shift of 1 m/s due to line deformation is detected as a 1.978 ± 0.100 m/s shift on average using *this* high-pass filter; whereas the slope for applying a low-pass filter is $k_{\text{L}} = 0.847 \pm 0.015$ ($\pm 1.8\%$). $RV_{\text{FT},\text{L}}$ is not as “responsive” as $RV_{\text{FT},\text{H}}$ to the line profile deformation, but returns a better constrained linearity. It’s also worth noting that the combined effect of these two

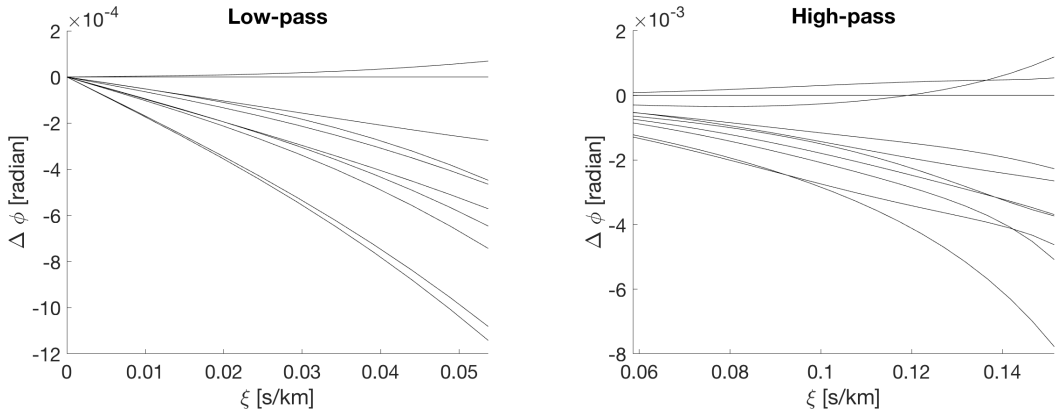


Fig. 2.12: Differential phase spectrum as shown in Fig. 2.10b sub-divided into lower frequency range and higher frequency range. Only the non-negative ranges are plotted for clarity.

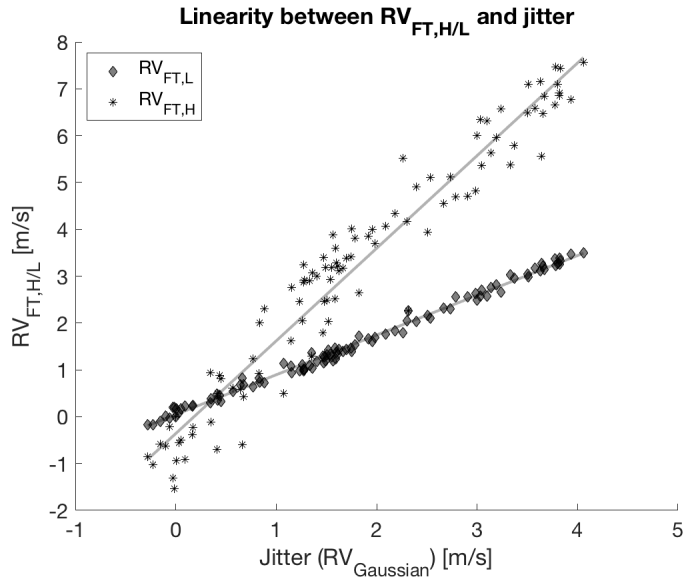


Fig. 2.13: Applying the low-pass and high-pass filters, the Fourier transform $RV_{FT,L}$ and $RV_{FT,H}$ are linearly correlated with the jitter ($RV_{Gaussian}$).

filters would have resulted in RV_{FT} , a consistent measurement of the radial velocity as with the fitting a line centroid as previously showed.

We can investigate how well this linearity behaves for each filter by scaling the measured $RV_{FT,L}$ and $RV_{FT,H}$ by their corresponding factors $1/k_L$ and $1/k_H$ respectively, and compare them with the jitter ($RV_{Gaussian}$), as presented in Fig. 2.14. The root-mean-squares of the residuals are $\sigma_{FT,L} \approx 0.11$ m/s and $\sigma_{FT,H} \approx 0.31$ m/s respectively. The reason for $\sigma_{FT,H} > \sigma_{FT,L}$ is the same as mentioned in §2.1.5 – higher frequency modes are more sensitive to noise, but the fact that both $\sigma_{FT,H/L}$ increase (opposed to $\sigma_{FT,H/L}$

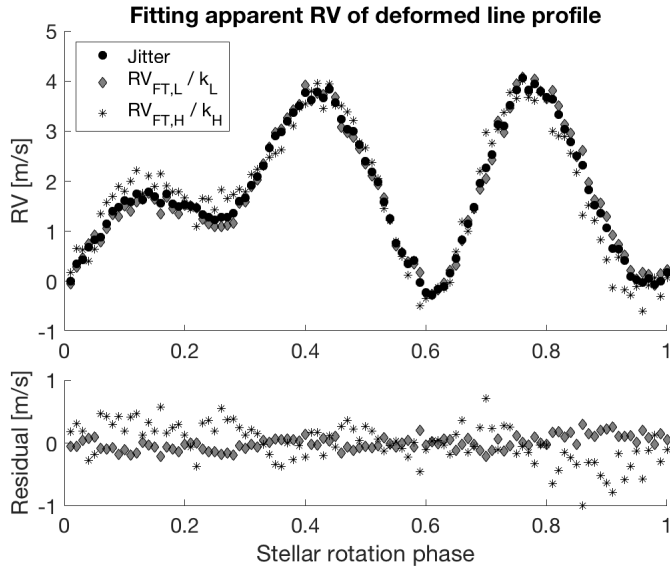


Fig. 2.14: Scaling the low-pass and high-pass Fourier transformed radial velocities to match the input jitter.

$= 0.08 \text{ m/s}$ in the case of a pure line shift) is because we think the linearity between $RV_{FT,H/L}$ and the input jitter is only empirically valid but not strictly followed. The deviation from linearity would affect how well we could recover the jitter by scaling $RV_{FT,H/L}$ and may also introduce systematics in the recovery of jitter.

2.2.4 Jitter model

We have shown in § 2.1 that the following measurable quantities demonstrate essentially the same response to pure line shifts: RV_{FT} , $RV_{FT,H/L}$ and RV_{Gaussian} . We have also shown in § 2.2 that both $RV_{FT,H}$ and $RV_{FT,L}$ are linearly correlated with the jitter, to which $RV_{FT,H}$ is more responsive ($k_H > 1$) than $RV_{FT,L}$ ($k_L < 1$).

We can therefore write the following measurable quantities – RV_{Gaussian} (or RV_{FT}), $RV_{FT,L}$ and $RV_{FT,H}$ – in the form of three additive terms: (1) a bulk shift in the star (which we hereafter assume to be due to a planet or planets as the superposition of Keplerian orbit(s)), (2) variability in the stellar line profile (hereafter lumped under the general name “jitter”), and (3) a constant radial velocity offset term chosen so as to be

absorbed into the previous two terms.

$$RV_{\text{Gaussian}} = RV_{\text{planet}} + RV_{\text{jitter}} \quad (2.11)$$

$$RV_{\text{FT,L}} = RV_{\text{planet}} + k_L \cdot RV_{\text{jitter}} \quad (2.12)$$

$$RV_{\text{FT,H}} = RV_{\text{planet}} + k_H \cdot RV_{\text{jitter}}. \quad (2.13)$$

Subtracting one from the other to remove RV_{planet} and reduce to two independent equations

$$RV_{\text{Gaussian}} - RV_{\text{FT,L}} = (1 - k_L) \cdot RV_{\text{jitter}} \quad (2.14)$$

$$RV_{\text{FT,H}} - RV_{\text{Gaussian}} = (k_H - 1) \cdot RV_{\text{jitter}} \quad (2.15)$$

Rearranging yields two expressions of the jitter model

$$RV_{\text{jitter}} = \frac{RV_{\text{Gaussian}} - RV_{\text{FT,L}}}{1 - k_L} \quad (2.16)$$

$$RV_{\text{jitter}} = \frac{RV_{\text{FT,H}} - RV_{\text{Gaussian}}}{k_H - 1} \quad (2.17)$$

where RV_{Gaussian} , $RV_{\text{FT,L}}$ and $RV_{\text{FT,H}}$ are direct measurements, whereas k_L and k_H are unknowns – we could determine k_L and k_H in the previously demonstrated simulations only because we knew there were no radial velocities other than jitter in the system. Dividing the two equations above further cancels RV_{jitter} , leaving

$$\frac{RV_{\text{Gaussian}} - RV_{\text{FT,L}}}{RV_{\text{FT,H}} - RV_{\text{Gaussian}}} = \frac{1 - k_L}{k_H - 1}, \quad (2.18)$$

which means $(1 - k_L)/(1 - k_H)$ can now be obtained by fitting a linear regression model on $(RV_{\text{Gaussian}} - RV_{\text{FT,L}})$ against $(RV_{\text{Gaussian}} - RV_{\text{FT,H}})$. With this, we rewrite the jitter model in a unified form – the weighted sum of the two jitter expressions from Eq. 2.16 and Eq. 2.17:

$$\begin{aligned} RV_{\text{jitter}} &= w_1 \frac{RV_{\text{Gaussian}} - RV_{\text{FT,L}}}{1 - k_L} + w_2 \frac{RV_{\text{FT,H}} - RV_{\text{Gaussian}}}{k_H - 1} \\ &= \frac{1}{k_H - 1} \left[w_1 \frac{RV_{\text{Gaussian}} - RV_{\text{FT,L}}}{\frac{1 - k_L}{k_H - 1}} + w_2 (RV_{\text{FT,H}} - RV_{\text{Gaussian}}) \right] \\ &= \alpha \left[w_1 \frac{RV_{\text{Gaussian}} - RV_{\text{FT,L}}}{\frac{1 - k_L}{k_H - 1}} + w_2 (RV_{\text{FT,H}} - RV_{\text{Gaussian}}) \right] \end{aligned} \quad (2.19)$$

in which the weights satisfy $w_1 + w_2 = 1$ and $1/(k_H - 1)$ is replaced by the scaling factor α in the last step.

An obvious check to implement is examining the correlation between $(RV_{\text{Gaussian}} - RV_{\text{FT,L}})$ and $(RV_{\text{FT,H}} - RV_{\text{Gaussian}})$ from Eq. 2.18 before going ahead with the jitter model (Eq. 2.16 and Eq. 2.17), because our jitter model is solely based on the empirically assumed linear response of $RV_{\text{FT,H/L}}$ to RV_{jitter} , either of which fails can be identified by plotting $(RV_{\text{Gaussian}} - RV_{\text{FT,L}})$ against $(RV_{\text{FT,H}} - RV_{\text{Gaussian}})$.

2.2.5 Testing the recovery of jitter

We performed tests to demonstrate the performance of recovering artificially generated jitter using this new technique (Eq. 2.19). We generated 200 deformed line profiles (in the form of cross-correlation functions) using SOAP 2.0. All the configurations are the same as used in §2.2.2, except that the data are produced from two rotation periods instead of one. The jitter amplitude is roughly 2 m/s. In addition, each line profile is further shifted by an amount RV_{planet} with an amplitude of the Keplerian orbit $A_{\text{planet}} = 2$ m/s (although in principle the RV_{planet} configuration shouldn't affect the jitter model because the term was cancelled out when we derived the jitter expression). The planetary orbital frequency to stellar rotation frequency ratio is set to be 0.7 (i.e. $\nu_{\text{orb}}/\nu_{\text{rot}} = P_{\text{rot}}/P_{\text{orb}} = 0.7$).

We then obtain three sets of radial velocities for each simulated profile: RV_{Gaussian} , $RV_{\text{FT,H}}$ and $RV_{\text{FT,L}}$ (Fig. 2.15 upper panel). We test three different combinations of w_1 and w_2 and apply a scaling factor α (fitted by linear regression to the known input jitter) to see how well it matches the input jitter: (1) $w_1 = 1, w_2 = 0$; (2) $w_1 = 0.5, w_2 = 0.5$; (3) $w_1 = 0, w_2 = 1$. The middle panel shows all these jitter models successfully recover adequate information of the input jitter, while presenting minor differences between them.

Weighted moving average At this stage, we implement a weighted moving average modulated by a Gaussian kernel to mitigate noise in the $RV_{\text{FT,H/L}}$ (excessive noise due to the sacrifice of frequency information) and the subsequent arithmetic. For N data points (e.g. radial velocities) v_i with an uncertainty σ_i observed at t_i ($i = 1, 2, \dots, N$), we define the contribution (i.e. weight) of a data point $(t_i, v_i \pm \sigma_i)$ towards the chosen position t as the multiplication of two factors: (1) the weight of the data point itself, inversely proportional to the uncertainty squared: $W_i = \frac{1}{\sigma_i^2}$ and (2) a stationary kernel that describes the correlation between data, depending on the distance $|t - t_i|$ and a time-scale of correlation τ : $K_i(t) = e^{-\frac{(t-t_i)^2}{2\tau^2}}$. With this, the evaluation of a data point

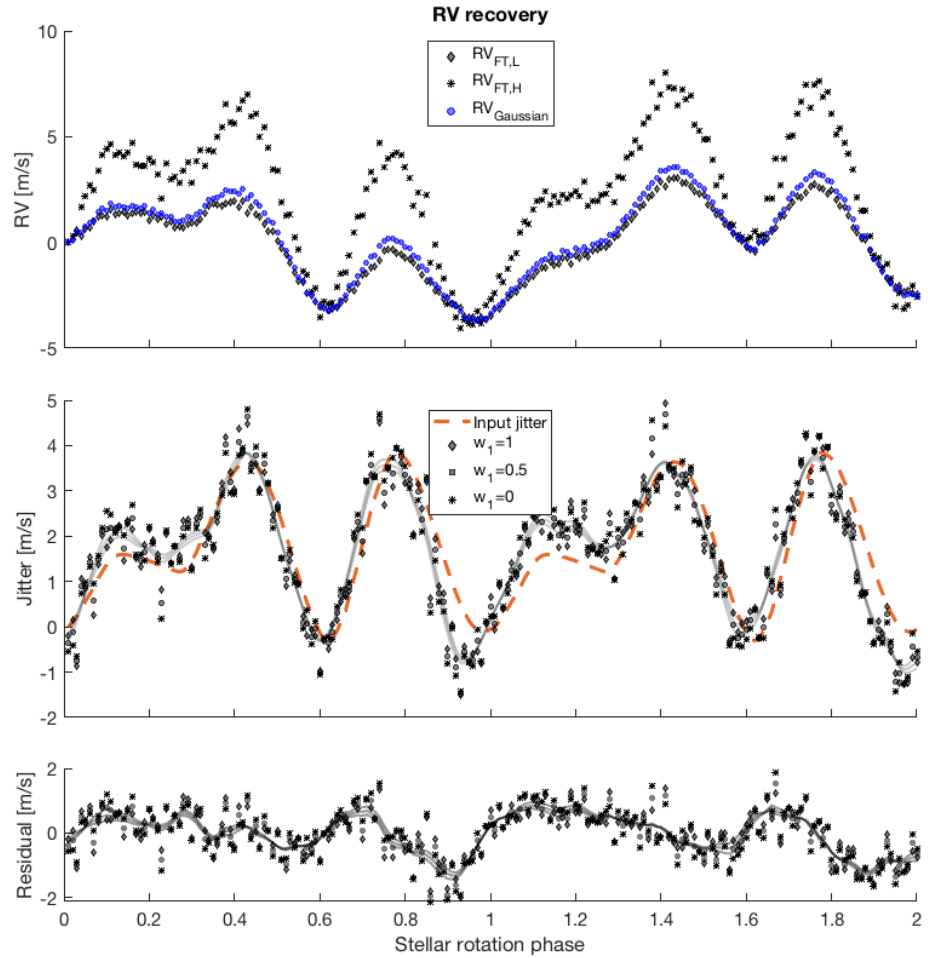


Fig. 2.15: Jitter recovery based on Eq. 2.19 for the simulated data ($S/N = 10,000$). Top: time series of directly measured RV_{Gaussian} and $RV_{\text{FT},\text{H/L}}$. Middle: three forms of the jitter expressions scaled by their respective factor α , smoothed by the weighted moving average (grey solid lines) with τ equal to the spacing of two samplings. For comparison, the input jitter is labelled as the orange dashed line. Bottom: difference between the jitter model and the input jitter, smoothed by the weighted moving average (grey solid lines).

$v(t)$ can be drawn by the weighted average of all observed data $(t_i, v_i \pm \sigma_i)$, with the weight

$$\mathbf{W}_i(t) = W_i \cdot K_i(t) = \frac{1}{\sigma_i^2} e^{-\frac{(t-t_i)^2}{2\tau^2}} \quad (2.20)$$

respectively and then normalised by the sum of weights, so that

$$v(t) = \frac{\sum_{i=1}^N [x_i * \mathbf{W}_i(t)]}{\sum_{i=1}^N \mathbf{W}_i(t)} \quad (2.21)$$

To quantitatively examine the performance of the jitter models, we compare the scatter of the residuals between the input jitter and the jitter models – σ_{residual} – with the scatter of the input jitter – $\sigma_{\text{jitter}} = 1.22$ m/s. The former can be treated as the scatter after the planets are correctly fitted and jitter is removed, whereas the latter are the scatter after fitting the correct planet(s) without jitter correction. We will see this example again in the following end-to-end simulations (§2.3). Table 2.2 lays out the scatter σ_{residual} for the raw jitter models and the smoothed jitter models implemented with the weighted moving average. In addition to the nearly noise-free ($S/N=10,000$) simulations, the corresponding simulations appropriate for real-world observations are presented in parallel. The chosen $S/N = 10,000$ is similar to that in the cross-correlation line profiles α Cen B observations from HARPS; S/N ranging from 2,000 to 4,000 are found in a dwarf star HD 189733 with apparent magnitude $V = 7.6$; $S/N \sim 1,000$ is found for red dwarfs Gl 176 and Wolf 1061 with $V \sim 10$.

	σ_{residual} (raw) [m/s]		σ_{residual} (smoothed) [m/s]	
	$S/N=10,000$	$S/N=2,000$	$S/N=10,000$	$S/N=2,000$
$w_1 = 1, w_2 = 0$	0.69	2.49	0.54	0.65
$w_1 = 0.5, w_2 = 0.5$	0.78	2.59	0.62	0.75
$w_1 = 0, w_2 = 1$	0.72	2.42	0.51	0.68

Table 2.2: Scatter of jitter residual (input $\sigma_{\text{jitter}} = 1.22$ m/s)

We note from the table, that the scatter of the input jitter is effectively reduced from 1.22 m/s to $\sigma_{\text{residual}} = 0.70$ m/s for $S/N=10,000$ but conversely doubled for $S/N=2,000$. Implementing the weighted moving average with a meaningful correlation time-scale τ (e.g. depend on the detail of information to be extracted from the data and the extent of noise to be flattened) can reduce the input jitter scatter σ_{jitter} by half in both cases. In this exercise, we choose the correlation time-scale for $S/N=10,000$

to be $\tau_{10000} = 0.01P_{rot}$, the distance between two cadence of simulated observations, and $\tau_{2000} = 5 \tau_{10000}$ for S/N=2,000 in order to further mitigate noise. We have also tested other smoothing approaches, such as the use of the Python package PyMC3 that implements Gaussian process in smoothing the data, which also returns similarly results.

Reaching sub-m/s in the residuals of fitting the jitter indicate the potential to enhance the detection of planets at sub-m/s precisions and reveal candidates with radial velocities of sub-m/s amplitudes even in the presence of stellar variability. However, this would require good sampling and we should not ignore there can be systematic differences between the actual jitter and our jitter models.

2.2.6 Planetary radial velocity recovery

In this subsection we discuss the possibilities to recover the radial velocity of the planet in a more direct way, though may not be as practical.

Having obtained the jitter model (Eq. 2.19) and knowing RV_{planet} follows a Keplerian orbital motion, we can turn our planetary radial velocity recovery into a model fitting problem, in which the parameters of the jitter model (such as the scaling factor) and that of the Keplerian orbit (such as amplitude, orbital period and phase) are to be determined.

Alternatively, we can bypass the jitter model. Revisiting the Equations 2.11-2.13, we rewrite them by observation number $i(i = 1, 2, \dots, N)$ and switch the notations to obtain the following $3N$ independent linear equations:

$$X_i = P_i + J_i \quad (2.22)$$

$$Y_i = P_i + k_y \cdot J_i \quad (2.23)$$

$$Z_i = P_i + k_z \cdot J_i \quad (2.24)$$

where X_i, Y_i and Z_i replace the three measurable radial velocities $RV_{\text{Gaussian}}, RV_{\text{FT,L}}$ and $RV_{\text{FT,H}}$; P_i and J_i are the planetary radial velocities and the jitter; k_y and k_z are the scaling factors k_L and k_H . Substituting $J_i = X_i - P_i$ from Eq. 2.22, we can simplify the system to the following $2N$ independent linear equations:

$$Y_i = k_y \cdot X_i + (1 - k_y)P_i \quad (2.25)$$

$$Z_i = k_z \cdot X_i + (1 - k_z)P_i. \quad (2.26)$$

The number of unknowns is $(N+4)$, including N from P_i , 2 from k_y and k_z , and another 2 from the previously absorbed constant offsets. Normally we have $N \gg 1$, so that the number of independent equations ($2N$) is larger than the number of degrees of freedom ($N+4$) in the system, meaning the system can be uniquely solved by optimization, such as least square minimization of the objective function:

$$\sum_{i=1}^N \left[w_{y,i} \left(k_y \cdot X_i + (1 - k_y) P_i - Y_i \right)^2 + w_{z,i} \left(k_z \cdot X_i + (1 - k_z) P_i - Z_i \right)^2 \right] \quad (2.27)$$

where $w_{y,i}$ and $w_{z,i}$ are pre-determined parameters (e.g. determined by the sizes of errorbars of the observed radial velocities) used to weight the linear systems. In addition, this approach becomes identical to constructing a jitter model (Eq. 2.19) in cases that (1) $w_{y,i} = 1, w_{z,i} = 0(i = 1, 2, \dots, N)$ and $w_1 = 1, w_2 = 0$; (2) $w_{y,i} = 0, w_{z,i} = 1(i = 1, 2, \dots, N)$ and $w_1 = 0, w_2 = 1$.

2.2.7 Conclusion

The Fourier phase spectrum analysis, when using (almost) all the information in the power spectrum and the phase spectrum, returns highly consistent radial velocities as the line centroid acquired by fitting a Gaussian profile. This consistency applies both for measuring a direct line shift and an apparent shift of a deformed line profile.

We believe the frequency dependent $x_0(\xi)$ is the key asset to identifying line profile deformation and distinguishing it from a bulk shift of a line. As far as we have investigated for a deformed line profile, the apparent radial velocity shift (i.e. jitter) can be seen as a mingle of two radial velocities – $RV_{FT,H}$ and $RV_{FT,L}$ – one in higher frequency modes the other in lower frequency modes. They are both, as obtained from the simulated spectral line profiles, scaled linearly with jitter.

The different linear responses of $RV_{FT,H}$ and $RV_{FT,L}$ enable us to construct a jitter model, which has reasonably recovered the simulated radial velocity data with stellar variability, both in our almost noise-free and real-world simulations.

2.3 End-to-end simulations

We run end-to-end simulations to test the performance of Φ ESTA on recovering the planetary candidate's signal in the presence of jitter. Specifically, we aim to answer the following three questions:

1. When the amplitude of jitter is comparable to that of planetary radial velocities, can we recover the planet orbital parameters better with our Φ ESTA?
2. When planetary radial velocities dominate and jitter is negligible, does Φ ESTA give at least equally good results as the traditional methods, i.e. without jitter correction?
3. When jitter is the only source of radial velocities, can it be identified with the help of Φ ESTA?

For all the following simulations, the spectral line profile simulator (SOAP 2.0) setup is the same as previously. The jitter amplitude is fixed at roughly 2 m/s, so we will adjust the planetary orbital amplitude to satisfy the three categories of end-to-end simulations. For S/N, we choose two numbers to represent the simulations: (1) S/N = 10,000 for super bright stars, where we will show its ability to make significant improvement using Φ ESTA on recovering the planetary signals when the star is active; (2) S/N = 2,000 where it starts to push the limit of Φ ESTA. We will run 500 trails, each trail with 60 randomly selected samples clustered in 12 groups, out of a total of 400 equally spaced samples from four stellar rotation periods.

The tests are divided into two main groups for comparison:

1. Fit RV_{Gaussian} by Keplerian orbit alone;
2. Fit RV_{Gaussian} by Keplerian orbit with jitter model correction. The following three variations of model fitting have been tested:
 - (a) Jitter model constructed with RV_{Gaussian} and $RV_{\text{FT,L}}$ only, i.e. $w_1 = 1$ and $w_2 = 0$;
 - (b) Jitter model constructed with RV_{Gaussian} and $RV_{\text{FT,H}}$ only, i.e. $w_1 = 0$ and $w_2 = 1$;
 - (c) Jitter model constructed with RV_{Gaussian} , $RV_{\text{FT,L}}$ and $RV_{\text{FT,H}}$, represented by $w_1 = 0.5$ and $w_2 = 0.5$ in our test.

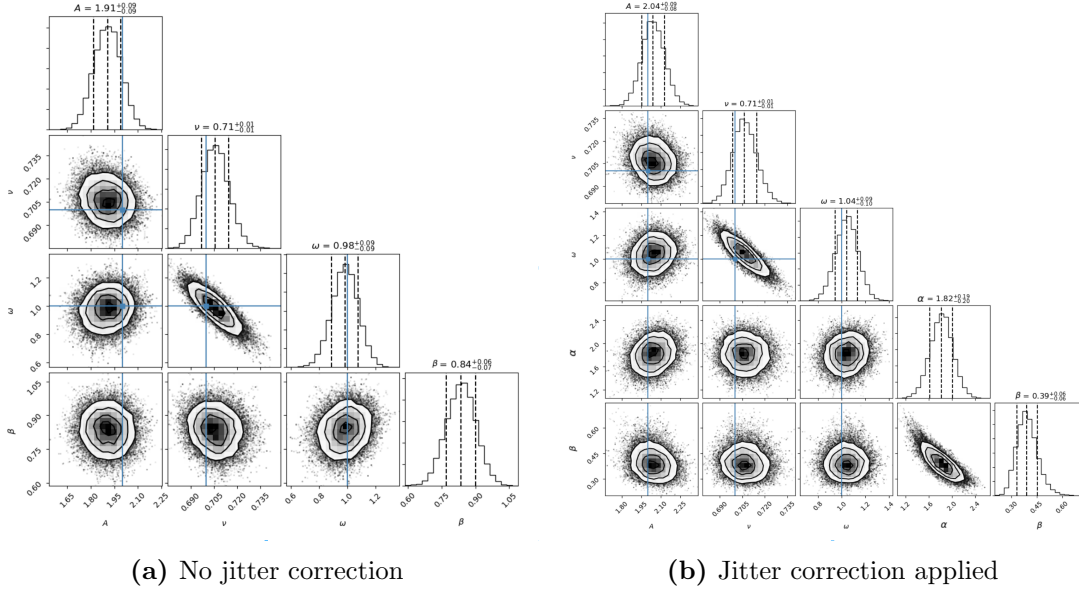


Fig. 2.16: Examples of two corner plots showing the successfully recovered planetary orbital parameters (within 10% of the true values) with MCMC sampling. The blue solid lines indicate the true values of the input orbital parameters. The three dashed lines of each histogram are the corresponding median and 1σ boundaries. A, ν, ω, α and β are the orbital amplitude, orbital frequency ratio, initial phase, the scaling factor for the jitter term and a radial velocity offset respectively.

The parameters for the fitting is obtained by Markov chain Monte Carlo (MCMC) sampling (such as shown in Fig. 2.16). Each radial velocity data is equally weighted as they have the same S/N in our simulation. We find that among the three variations of jitter correction treatments, the one left with the least residual (i.e. smallest rms) empirically returns the best fitting parameters, which we would use to represent the fitting from Group 2.

2.3.1 Stellar jitter as strong as planetary signal

The injected planet has the same parameter settings as in §2.2.5, i.e. circular orbit with amplitude $A = 2$ m/s, orbital frequency ratio $\nu = \nu_{\text{orb}}/\nu_{\text{rot}} = 0.7$ and initial phase $\omega = 1$ rad. For demonstration, we present two snapshots of each of the 500 trials of end-to-end simulations, with one $S/N = 10,000$ and the other $S/N = 2,000$ (Fig. 2.17). These are two examples where the planetary orbital parameters are correctly recovered (within 10% of the true values in this case). For $S/N = 10,000$, the discrepancy between the simulated radial velocities and the planet model is accounted for by the jitter model, and thus applying the jitter correction significantly reduces the rms of the residual. For

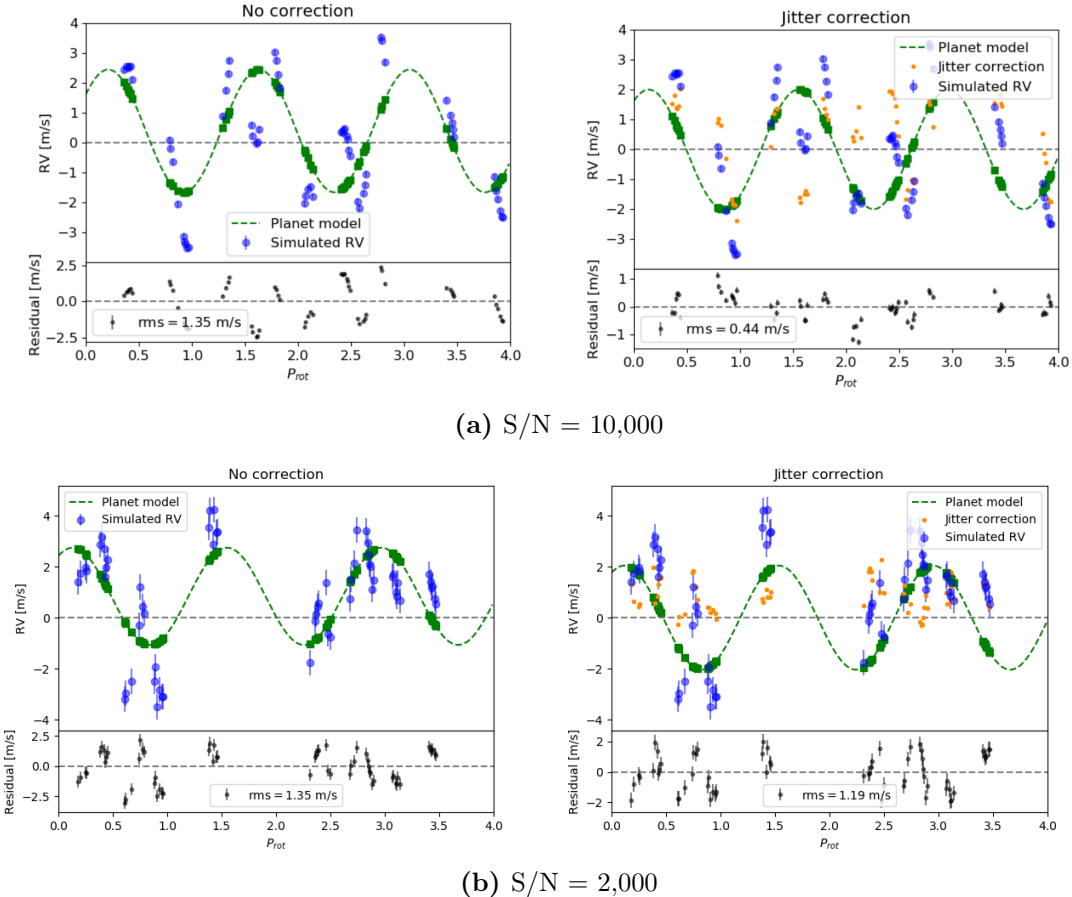


Fig. 2.17: One of the 500 trials of radial velocity fitting for $A = 2 \text{ m/s}$ for $\text{S/N} = 10,000$ and 2,000 respectively.

$\text{S/N} = 2,000$, the fitting is only slightly improved introducing jitter correction. The jitter model is not as accurate in the presence of moderate noise.

In the end, we obtain the histograms of the recovered orbital parameters for a total of 500 runs (Fig. 2.18). To quantitatively describe their performances, we calculate the percentage of parameters successfully recovered within 5% and 10% of the true values as summarized in Table 2.3. For example, for $\text{S/N} = 10,000$, 46% of the 500 trials have both the amplitude (A) and orbital frequency ($\nu_{\text{orb}}/\nu_{\text{rot}}$) successfully recovered within 5% of the true parameters with jitter correction applied, while only 8% of them achieve such a precision without jitter correction.

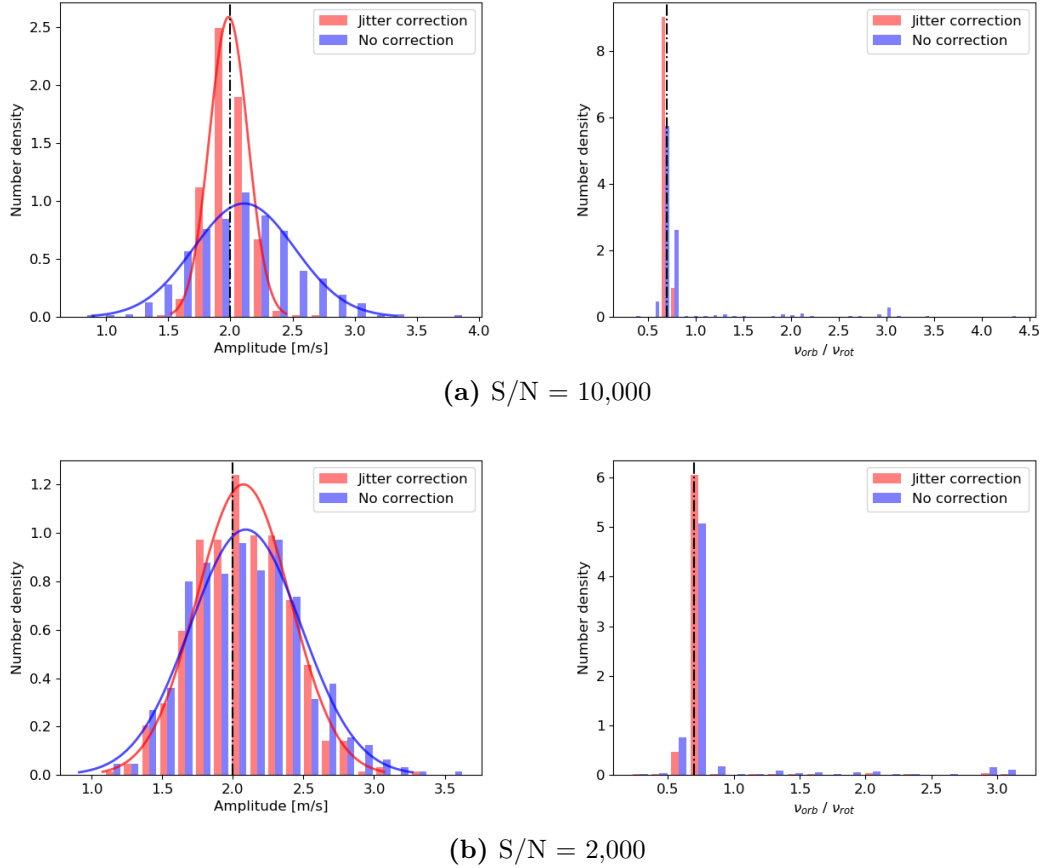


Fig. 2.18: Histograms of recovered orbital parameters with a Gaussian profile fitted on top (where applicable).

Percentage	$S/N = 10,000$				$S/N = 2,000$			
	5% limit		10% limit		5% limit		10% limit	
	†	‡	†	‡	†	‡	†	‡
A	18%	50%	37%	79%	20%	23%	37%	42%
$\nu_{\text{orb}}/\nu_{\text{rot}}$	53%	93%	78%	100%	49%	66%	77%	91%
both A and $\nu_{\text{orb}}/\nu_{\text{rot}}$	8%	46%	27%	79%	10%	16%	28%	38%

Table 2.3: Proportion of recovered parameters within 5% and 10% limit of $A = 2 \text{ m/s}$ and $\nu_{\text{orb}}/\nu_{\text{rot}} = 0.7$. †: no correction; ‡: jitter correction applied.

2.3.2 Planetary signal dominates

In this case, we set the orbital amplitude roughly 10 times as strong as the jitter, i.e. $A = 20 \text{ m/s}$ (Fig. 2.19). Although both with and without the aid of jitter correction manage

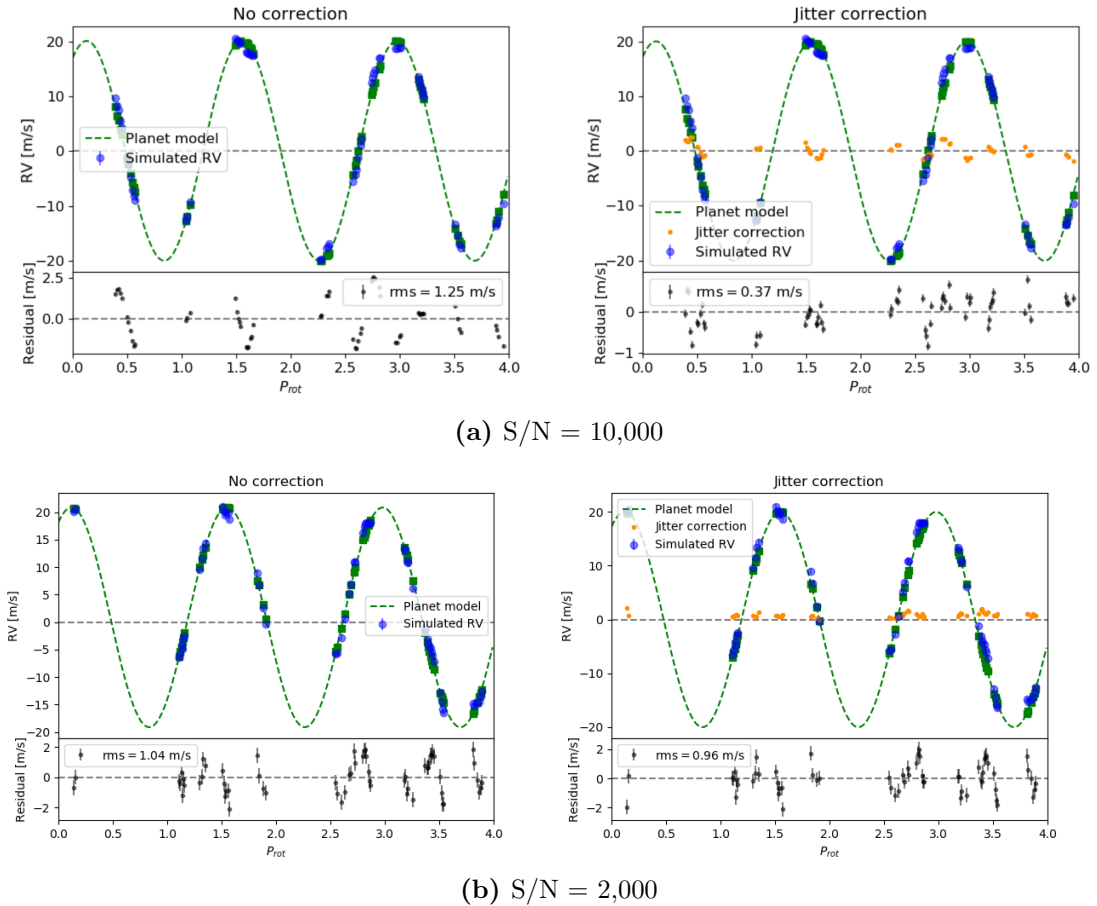


Fig. 2.19: Same with Fig. 2.17 but for $A = 20$ m/s.

to recover the planetary orbital parameters accurately enough, implementing Φ ESTA further improves the performance, especially in high S/N (Fig. 2.20 and Table. 2.4).

Percentage	S/N = 10,000				S/N = 2,000			
	1% limit		5% limit		1% limit		5% limit	
	†	‡	†	‡	†	‡	†	‡
A	33%	61%	99%	100%	34%	40%	98%	100%
$\nu_{\text{orb}}/\nu_{\text{rot}}$	92%	100%	100%	100%	93%	96%	100%	100%
both A and $\nu_{\text{orb}}/\nu_{\text{rot}}$	30%	61%	99%	100%	31%	38%	98%	100%

Table 2.4: Proportion of recovered parameters within 1% and 5% limit of $A = 20$ m/s and $\nu_{\text{orb}}/\nu_{\text{rot}} = 0.7$. †: no correction; ‡: jitter correction applied.

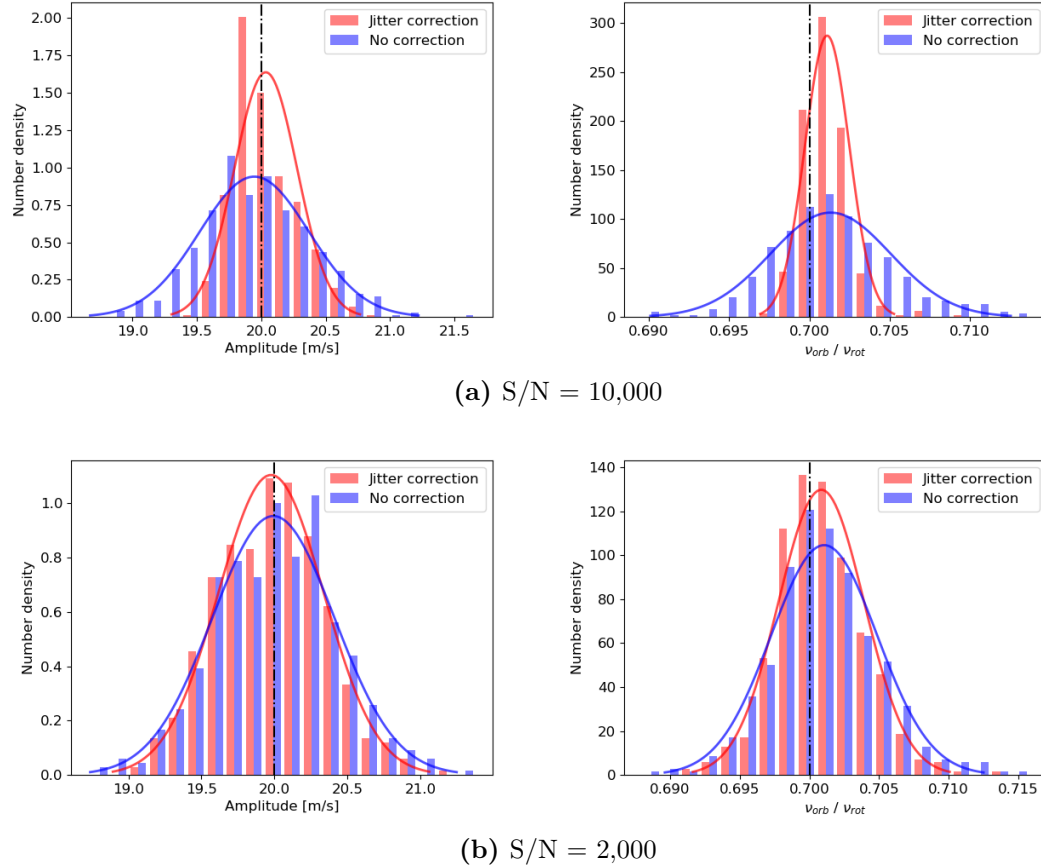


Fig. 2.20: Same with Fig. 2.18 but for $A = 20 \text{ m/s}$.

2.3.3 Stellar jitter only

We set $A = 0 \text{ m/s}$ so that the measured the radial velocity only comes from stellar variability. We implement the same approaches as above to see if the applying the jitter correction can return a null planet solution i.e. recovered amplitude smaller than the noise level.

We remind ourselves that the spot configuration in Table 2.1 is used. Three starspots appear and disappear in turns (Fig. 2.11), mimicking the radial velocities of orbiting exoplanets. This is indeed the case in the histogram of “recovered” orbital parameters (Fig. 2.21) – three peaks occur at $\nu_{\text{orb}}/\nu_{\text{rot}} = 1, 2$ and 3 , with $\nu_{\text{orb}}/\nu_{\text{rot}} = 3$ being the most prominent. Applying the jitter correction, the amplitudes of the “recovered” planet for $S/N = 10,000$ is effectively reduced, but its performance is only marginally better for $S/N = 2,000$, and neither of them reaches below the rms of photon noise level: $\sim 0.1 \text{ m/s}$ for $S/N = 10,000$ and $\sim 0.5 \text{ m/s}$ for $S/N = 2,000$. We still cannot

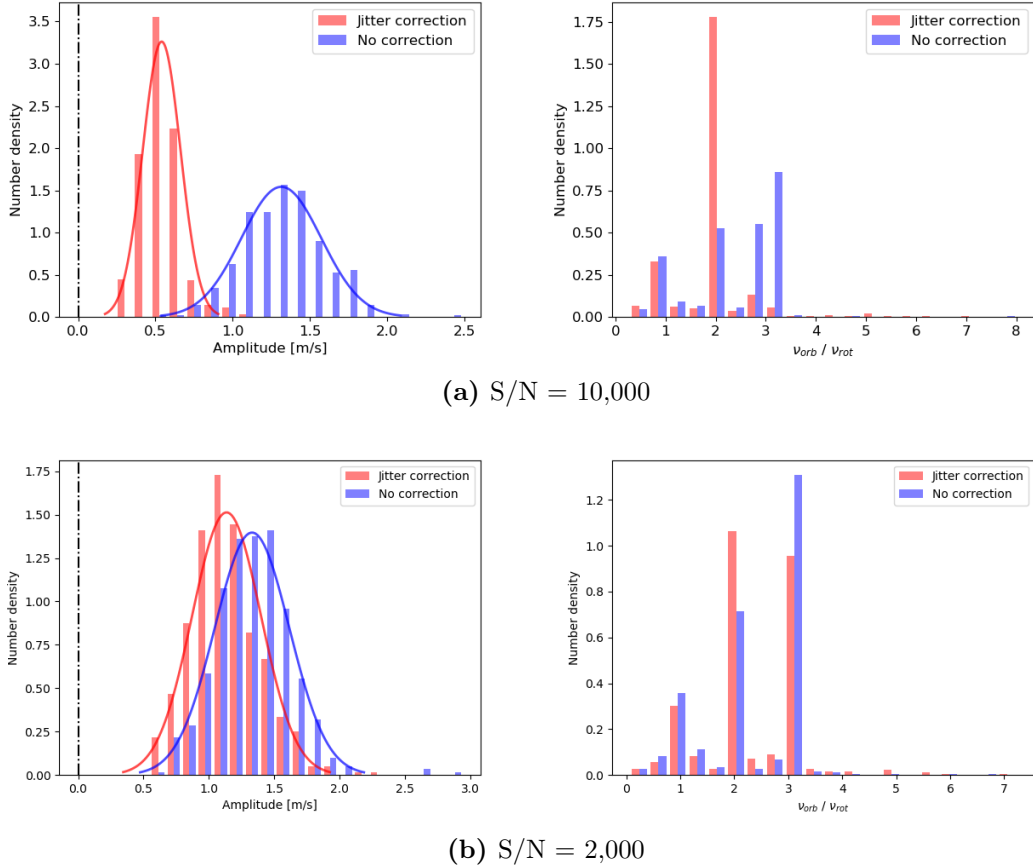
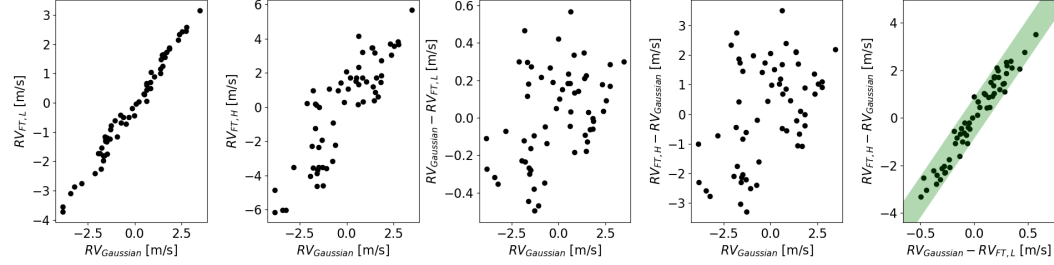


Fig. 2.21: Histogram of “recovered” orbital parameters in null planet end-to-end simulations.

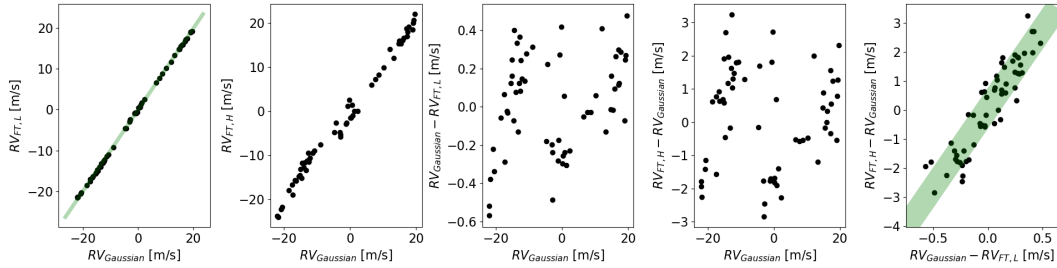
completely rule out the possibility of a reduced amplitude being true. Therefore, we come up with the following two subsections to discuss how we can classify whether the planetary signal or the stellar jitter dominates the observed radial velocities.

2.3.4 Classification

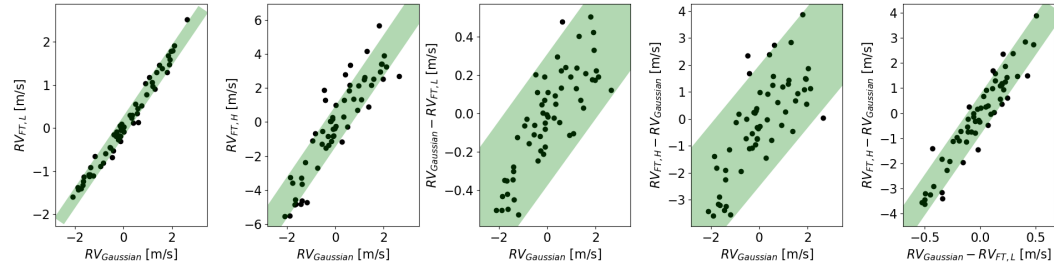
We demonstrate the use of the difference in the correlations among RV_{Gaussian} , $RV_{\text{FT,H,L}}$ and their combinations as to classify the three scenarios of different relative sizes between the jitter and planetary signals. The discussions are within the captions of Fig. 2.22.



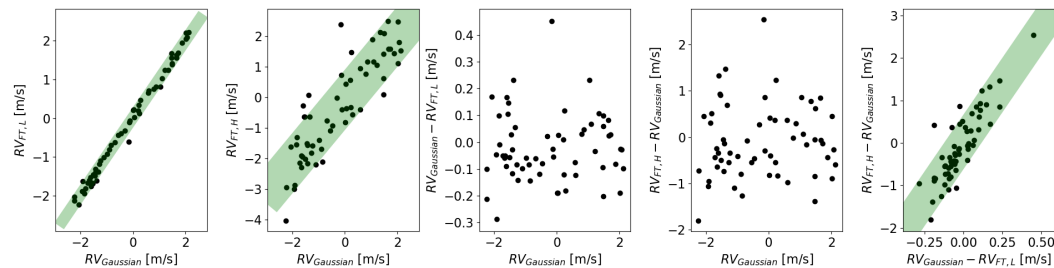
(a) Stellar jitter as strong as planetary signal: featured by (1) a decent correlation between RV_{Gaussian} and $RV_{\text{FT},L}$ and (2) no correlation between $RV_{\text{Gaussian}} - RV_{\text{FT},H,L}$.



(b) Planetary signal dominating: featured by (1) a tight correlation between $RV_{\text{FT},L}$ and RV_{Gaussian} and (2) no correlation between $RV_{\text{Gaussian}} - RV_{\text{FT},H,L}$.



(c) Jitter only; no planet: featured by linear correlations in all the subplots, on which ΦESTA are based.



(d) Planet only; “no” jitter. No apparent difference from (a) at first sight. This is because ΦESTA cannot tell whether the difference between line profiles are due to what we define as stellar jitter or the fluctuation from photon noise, but notice the scales of $RV_{\text{FT},H,L}$ in (d) are different from (a), because $RV_{\text{FT},H} \approx RV_{\text{FT},L} \approx RV_{\text{Gaussian}}$ without the presence of jitter.

Fig. 2.22: Classification of a system whether it’s jitter dominated or planetary signal dominated.

2.3.5 Periogodgram combined with the Φ ESTA

We would use the generalized Lomb-Scargle periodogram [2] in combination with Φ ESTA to address the problem of stellar jitter mimicking planetary signals. The idea is to compare the periodogram of the measured radial velocity (i.e. RV_{Gaussian}) and that of the proto-jitter (i.e. $|RV_{\text{FT},H/L} - RV_{\text{Gaussian}}|$). Peaks of the periodogram in the former are possible candidates whereas the latter would indicate jitter.

Fig. 2.23 demonstrates the application of periogodgram together with Φ ESTA, on the well sampled radial velocities (without sub-sampling) from the two end-to-end simulations in §2.3: (1) stellar jitter as strong as planetary signal and (2) stellar jitter only. The S/N of the cross-correlation profile is 2000 and because we used a full range of sampling, no moving average was applied. In Fig. 2.23a the planetary orbital frequency $\nu_{\text{orb}}/\nu_{\text{rot}} = 0.7$ clearly stands out while the other peaks coincide with that of the proto-jitter. It effectively shows, the proto-jitter model generated by Φ ESTA manages to disentangle jitter from the planetary component of the radial velocities (we recall that the planetary radial velocity was cancelled out to construct the jitter model). In the case of a null planet (Fig. 2.23b), all the possible candidates where the RV_{Gaussian} peaks occur are negated by the same detected periodicity of the jitter.

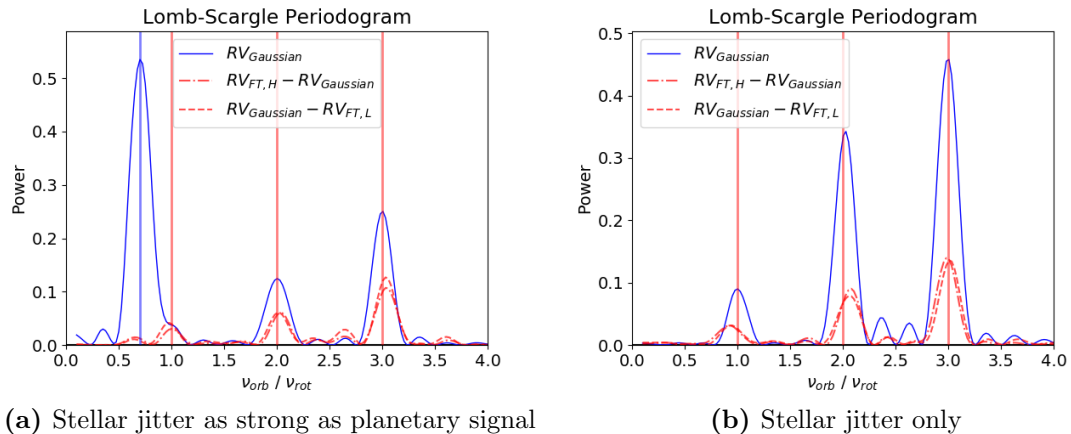


Fig. 2.23: Periodogram of RV_{Gaussian} and $|RV_{\text{FT},H/L} - RV_{\text{Gaussian}}|$. The single prominent peak in (a) indicates the orbital frequency (or period) of the injected planet. The true orbital frequency is labelled as the blue vertical line; the suspicious frequencies are labelled in red vertical lines at $\nu_{\text{orb}}/\nu_{\text{rot}} = 1, 2$ and 3 .

2.4 Applying Φ ESTA on real observations

2.4.1 HD189733: Rossiter–McLaughlin effect as jitter

HD189733 is a well studied binary star system. The main star HD189733 A is known to host a gas giant exoplanet HD189733 b, first detected by transits and followed by Doppler spectroscopy confirmation [3]. Its Rossiter–McLaughlin effect (Fig. 2.24), as a change in radial velocities when the planet passes in front of its parent star, was studied by [4] and [5]. During the eclipse, the planet breaks the observed flux symmetry of the stellar photosphere, resulting in imbalanced redshift and blueshift, producing an asymmetric spectral line profile and apparent radial velocity shifts.

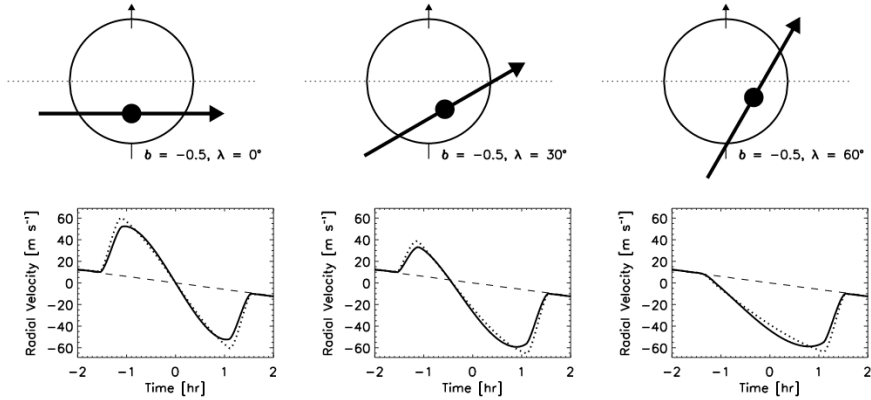


Fig. 2.24: Demo: Rossiter–McLaughlin effect (figure taken from [6]). It is an apparent radial velocity change of the parent star due to an eclipsing binary (whether star or planet) in front of the stellar photosphere. It shows in this plot three different star–planet alignments that cause three corresponding different forms of Rossiter–McLaughlin curves. Solid line is the model with limb darkening as opposed to dotted line without limb darkening.

We aim to test if our jitter model generated by Φ ESTA can account for the apparent radial velocity shift as a result of Rossiter–McLaughlin effect. We choose this target as a case study for the following reasons: (1) HD189733 b is a confirmed transiting exoplanet, so that we know what to expect from the radial velocity shift during the eclipse. (2) The gas giant exoplanet causes a prominent apparent radial velocity shift while it transits (amplitude up to ~ 40 m/s) arising from Rossiter–McLaughlin effect, making it the dominant factor of the radial velocity shift, although the star itself exhibits signs of activity ([7], [8]). (3) The system HD189733 has a visual magnitude of $V \sim 7.65$ [9] (or $G = 7.41$ from the Gaia archive), dominated by the primary host

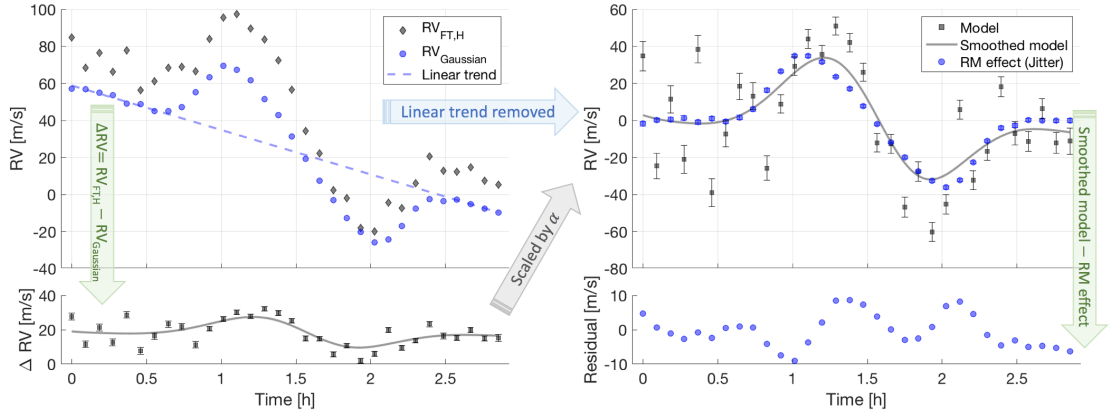


Fig. 2.25: Flowchart of modelling Rossiter–McLaughlin effect as jitter using Φ ESTA on HD189733. Note that the errorbars related to the radial velocities from Φ ESTA (e.g. the scaled raw jitter in the top right panel) are correct in scale relative to each other (as derived from the photon noise) but not evaluated in the absolute value.

star HD189733 A, with a relatively high S/N in the HARPS cross-correlation profile, enabling decently good performance of Φ ESTA in recovering radial velocities.

Here we briefly recap the procedure of obtaining the “jitter” model by Φ ESTA. Both RV_{Gaussian} , $RV_{\text{FT},\text{H}}$ and $RV_{\text{FT},\text{L}}$) are calculated from the HARPS cross-correlation of the spectral lines. Note that RV_{Gaussian} , RV_{HARPS} and RV_{FT} deliver consistent radial velocities, and thus in practice, it barely makes difference to adopt any of them as the radial velocity shift of the line profile. We calculate $\Delta RV = |RV_{\text{Gaussian}} - RV_{\text{FT},\text{H/L}}|$ as the raw proto-jitter (Fig. 2.25 bottom left). We know that during transit, the orbital phase of the planet HD189733 b is zero and thus contributes no radial velocity, however, the inclined trend of the radial velocity curve is attributed to the exoplanet whose orbital period is estimated 11 days [3], as well as the other star HD189733 B in the binary star system of which the orbital period is estimated around 3,200 years [10], both being reasonably long enough as opposed to the time-scale of the planetary transit of hours, therefore a local linear approximation can be applied by fitting a linear trend onto the non-transiting part of the radial velocities as the orbital radial velocities, which is then removed and left with the Rossiter–McLaughlin curve (Fig. 2.25 top right). It can be now treated as “jitter” and modelled by the raw proto-jitter multiplied by a scaling factor (Fig. 2.25 right).

For this exercise, the scaled model is smoothed by the weighted moving average with $\tau \sim 0.2$ hour, twice of the spacing of two consecutive observations. Despite

mitigating against additional noise brought by ϕ ESTA, it smears the drastic velocity change when the planet ingresses and egresses the stellar disk. Applying a correct Rossiter–McLaughlin curve model is expected to improve the fitting, we still adopt the smoothing approach the way we would normally (intend to) deal with stellar variability induced radial velocities instead, to demonstrate the sufficiently recovered radial velocities as a result of line profile deformation – a 75% removal of the “jitter” from ~ 40 m/s to ~ 10 m/s.

2.4.2 α Centauri B (HD128621)

We chose α Centauri B as our case study for its brightness ($V \sim 1.33$), abundant HARPS observations, and the controversy over whether it hosts an exoplanet due to its intrinsic stellar activity. Being potentially the (second) closest exoplanet to Earth, the candidate α Centauri B was first discovered by [11] in 2012, then further investigated by [12] in 2013, and later questioned by [13], suggesting the ghost signal arised from the window function. We haven’t gone as far as probing the spurious planetary candidate, but we could study is the stellar activity level of α Centauri B, presented by a scaled jitter correction $| RV_{\text{HARPS}} - RV_{\text{FT,H/L}} |$. In the following, we focus on three segments of the α Centauri B data sets for activity analysis, each roughly one year apart, spanning within three months and including over 2000 observations. Epoch 1: 15/02/2009 - 06/05/2009; Epoch 2: 03/23/2010 - 12/06/2010; Epoch 3: 18/02/2011 - 15/05/2011. Among them, Epoch 2 is of particular interest as it has been used to study rotationally modulated stellar activities in K-dwarfs ([14], [15]).

We downloaded 2617 α Centauri B spectra for Epoch 2 (2010) from the ESO archive, from which we selected the 2529 cross-correlation line profiles that were constructed with a K5 stellar template; the number of observations actually used was then further reduced to 2488 as we took out another 41 observations that presented large radial velocity offsets and visually different cross-correlation line profiles compared with the rest of the profiles. These removed observations had features at ephemeral time-scales, i.e. their radial velocities stood out from the other observations of the same day in the RV_{HARPS} or $| RV_{\text{HARPS}} - RV_{\text{FT,H/L}} |$ time-series and they were also classified as outliers in the full width at half maximum (FWHM) indicator, suggesting the presence of stellar flares. Epoch 1 (2009) and 3 (2011) were pre-filtered in a similar manner, resulting in 2220 and 3534 observations used respectively.

Fig. 2.26 presents the results of Φ ESTA analysis of $\Delta RV_L = RV_{\text{HARPS}} - RV_{\text{FT,L}}$ for these 3 years. $\Delta RV_H = RV_{\text{FT,H}} - RV_{\text{HARPS}}$ is not shown here as it is simply proportional to ΔRV_L and works the same way. We fit ΔRV_L with a Gaussian process model described by a quasi-periodic kernel. A Gaussian process model has the advantage of interpreting stochastic processes with a set of flexible forms of functions, constrained by physically motivated covariance kernels. In this case, a quasi-periodic kernel was chosen such that the periodicity can be explained by the rotationally modulated activity and the deviation from periodicity explained by possibly self-evolving disc features (e.g. starspots and plage, differential rotation). Interested readers can refer the theoretical background of Gaussian processes to a textbook-like literature [16] or a hitchhiker’s guide to Gaussian processes for time-series modelling [17]. For the implementation of the Gaussian process model, we employed the python library `george` developed by Foreman-Mackey [18].

The figure shows the star’s activity level increased dramatically from 2009 (upper panel) to 2010 (middle panel), and then declined in 2011 (lower panel). It indicates in 2010, α Centauri B was dominated by a simple global feature on the stellar surface that appeared at a rotation period of around 40 days, while in 2009 and 2011 the star might be covered by various local features, making the disc inhomogeneous at smaller scales. A substantial literature have studied and even modelled the rotational activity in an attempt to pin down the exoplanet candidate α Centauri Bb, so that we can compare our results with them. The prominent periodicity in 2010 is found to be consistent with $\log(R'_{HK})$ in original discovery paper [11], as well as the equivalent widths and core flux of activity-sensitive Fe and Mg lines reported in [14] and [15]. While our scaled jitter correction ΔRV_L in Epoch 2 (2010) does not match with rotational activity fit from [11] and [12], we do find some similarities shared between our ΔRV_L in Epoch 3 (2011) and the corresponding trunk of rotational activity fit presented in [11] and [12], which were obtained using completely different methods from ours.

We obtained the stellar rotation period from the best fit solution with a quasi-periodic kernel. For the three phases that we studied from 2009 to 2011, the rotation period is estimated to be 37.05, 35.70 and 36.71 days, all within 1σ of the pre-claimed 36.2 ± 1.4 days [19]; the rotation period of Epoch 3 (2011) that we obtained is highly consistent with the one from [11]. Unsurprisingly, the other two periods are not, as our ΔRV_L model is different from the activity model fit in [11].

While , §2.3.4 has demonstrated Φ ESTA does provide a quick assessment of whether a system hosts a planet / planets.

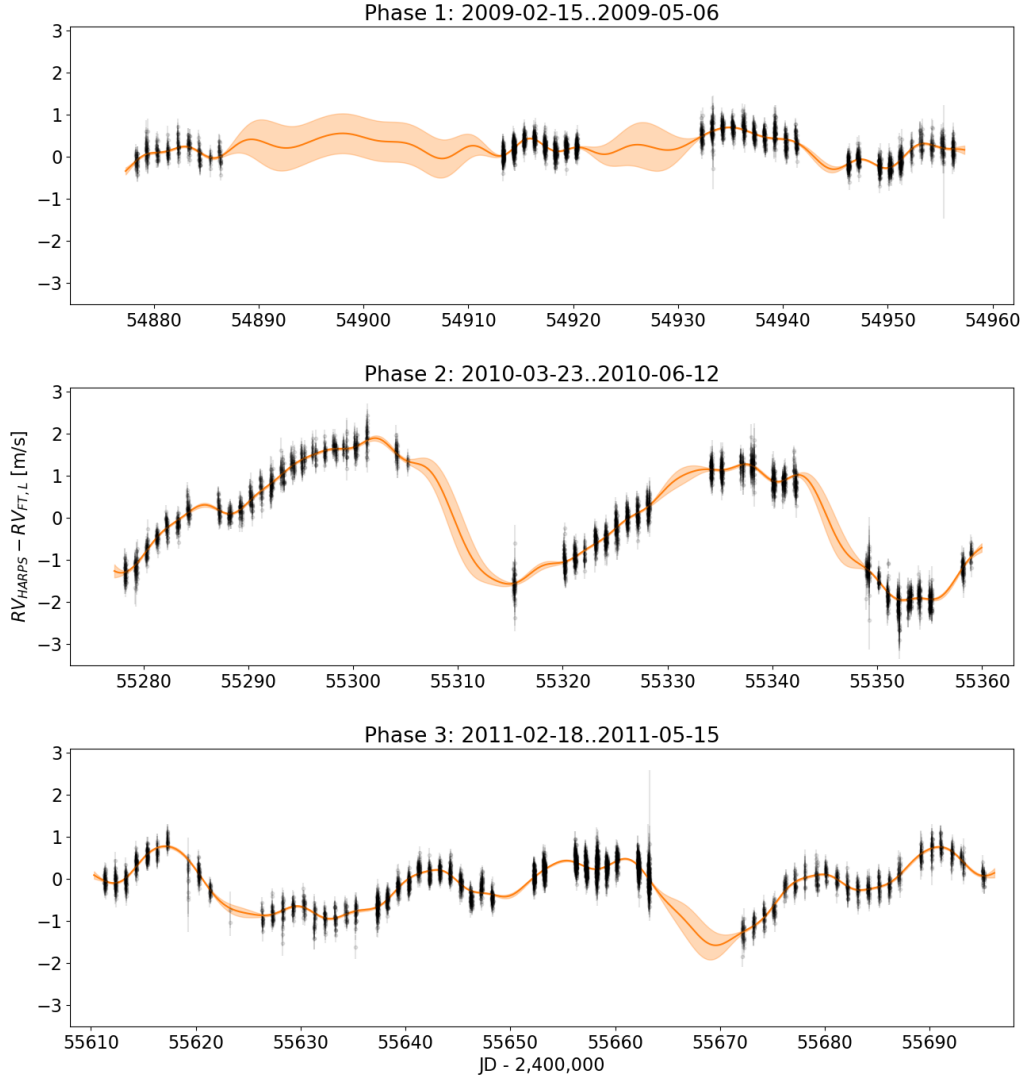


Fig. 2.26: Stellar activity analysis of α Centauri B using Φ ESTA. The scaling of the corresponding axes on all subplots are identical. Black dots with errorbars are radial velocities $RV_{\text{HARPS}} - RV_{\text{FT,L}}$; the orange solid line is the best fit solution with a quasi-periodic kernel using Gaussian processes and the shaded area is its 1σ boundary.

2.4.3 ϵ Eridani (HD22049)

2.4.4 τ Ceti (HD10700)

2.5 References

- [1] X. Dumusque, I. Boisse, and N. C. Santos. Soap 2.0: A tool to estimate the photometric and radial velocity variations induced by stellar spots and plages. *The Astrophysical Journal*, 796(2):132, 2014. 8
- [2] Zechmeister, M. and Kürster, M. The generalised lomb-scargle periodogram - a new formalism for the floating-mean and keplerian periodograms. *A&A*, 496(2):577–584, 2009. 35
- [3] Bouchy, F., Udry, S., Mayor, M., Moutou, C., Pont, F., Iribarne, N., Da Silva, R., Illovaisky, S., Queloz, D., Santos, N. C., Ségransan, D., and Zucker, S. Elodie metallicity-biased search for transiting hot jupiters - ii. a very hot jupiter transiting the bright k star hd189733. *A&A*, 444(1):L15–L19, 2005. 36, 37
- [4] W. D. Cochran, M. Endl, R. A. Wittenmyer, and A. P. Hatzes. The Rossiter-McLaughlin Effect In Transits Of The Planet Hd189733b. In *AAS/Division for Planetary Sciences Meeting Abstracts #38*, volume 38 of *Bulletin of the American Astronomical Society*, page 481, September 2006. 36
- [5] Triaud, A. H. M. J., Queloz, D., Bouchy, F., Moutou, C., Cameron, A. C., Claret, A., Barge, P., Benz, W., Deleuil, M., Guillot, T., Hébrard, G., Lecavelier des Étangs, A., Lovis, C., Mayor, M., Pepe, F., and Udry, S. The rossiter-mclaughlin effect of corot-3b and hd189733b. *A&A*, 506(1):377–384, 2009. 36
- [6] B. Scott Gaudi and Joshua N. Winn. Prospects for the characterization and confirmation of transiting exoplanets via the rossiter-mclaughlin effect. *The Astrophysical Journal*, 655(1):550, 2007. 36
- [7] Boisse, I., Moutou, C., Vidal-Madjar, A., Bouchy, F., Pont, F., Hébrard, G., Bonfils, X., Croll, B., Delfosse, X., Desort, M., Forveille, T., Lagrange, A.-M., Loeillet, B., Lovis, C., Matthews, J. M., Mayor, M., Pepe, F., Perrier, C., Queloz, D., Rowe, J. F., Santos, N. C., Ségransan, D., and Udry, S. Stellar activity of planetary host star hd 189733. *A&A*, 495(3):959–966, 2009. 36
- [8] P. Wilson Cauley, Seth Redfield, and Adam G. Jensen. A decade of h alpha transits for hd 189733 b: Stellar activity versus absorption in the extended atmosphere. *The Astronomical Journal*, 153(5):217, 2017. 36
- [9] C. Koen, D. Kilkenny, F. van Wyk, and F. Marang. Ubv(ri)cjhk observations of hipparcos-selected nearby stars. *Monthly Notices of the Royal Astronomical Society*, 403(4):1949–1968, 2010. 36
- [10] Gáspár Á. Bakos, András Pál, David W. Latham, Robert W. Noyes, and Robert P. Stefanik. A stellar companion in the hd 189733 system with a known transiting extrasolar planet. *The Astrophysical Journal Letters*, 641(1):L57, 2006. 37
- [11] Xavier Dumusque, Francesco Pepe, Christophe Lovis, Damien Ségransan, Johannes Sahlmann, Willy Benz, François Bouchy, Michel Mayor, Didier Queloz, Nuno Santos, and Stéphane Udry. An earth-mass planet orbiting α centauri b. *Nature*, 491:207 EP –, 10 2012. 38, 39

- [12] Artie P. Hatzes. The radial velocity detection of earth-mass planets in the presence of activity noise: The case of alpha centauri bb. *The Astrophysical Journal*, 770(2):133, 2013. 38, 39
- [13] V. Rajpaul, S. Aigrain, and S. Roberts. Ghost in the time series: no planet for alpha cen b. *Monthly Notices of the Royal Astronomical Society: Letters*, 456(1):L6–L10, 2016. 38
- [14] A. P. G. Thompson, C. A. Watson, E. J. W. de Mooij, and D. B. Jess. The changing face of α centauri b: probing plage and stellar activity in k dwarfs. *Monthly Notices of the Royal Astronomical Society: Letters*, 468(1):L16–L20, 2017. 38, 39
- [15] A. W. Wise, S. E. Dodson-Robinson, K. Bevenour, and A. Provini. New methods for finding activity-sensitive spectral lines: Combined visual identification and an automated pipeline find a set of 40 activity indicators. *The Astronomical Journal*, 156(4):180, 2018. 38, 39
- [16] CE Rasmussen and CKI Williams. *Gaussian Processes for Machine Learning*. Adaptive Computation and Machine Learning. MIT Press, Cambridge, MA, USA, 1 2006. 39
- [17] S. Roberts, M. Osborne, M. Ebden, S. Reece, N. Gibson, and S. Aigrain. Gaussian processes for timeseries modelling. *Philosophical Transactions of the Royal Society (Part A)*. 39
- [18] S. Ambikasaran, D. Foreman-Mackey, L. Greengard, D. W. Hogg, and M. O’Neil. Fast Direct Methods for Gaussian Processes. March 2014. 39
- [19] L. E. DeWarf, K. M. Datin, and E. F. Guinan. X-ray, fuv, and uv observations of alpha centauri b: Determination of long-term magnetic activity cycle and rotation period. *The Astrophysical Journal*, 722(1):343, 2010. 39

